
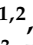







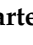
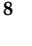



## Article

# Magnetic CuFe<sub>2</sub>O<sub>4</sub> Nanoparticles Immobilized on Modified Rice Husk-Derived Zeolite for Chlorogenic Acid Adsorption

Tainara Ramos Neves <sup>1,2,\*</sup>, Leticia Ferreira Lacerda Schildt <sup>1,2</sup>, Maria Luiza Lopes Sierra e Silva <sup>1,2</sup>, Vannyla Viktória Viana Vasconcelos <sup>1,2</sup>, Corrado Di Conzo <sup>3</sup>, Francesco Mura <sup>4</sup>, Marco Rossi <sup>4</sup>, Gaspare Varvaro <sup>5</sup>, Maryam Abdolrahimi <sup>5,6</sup>, Simone Quaranta <sup>7</sup>, Sandra Aparecida Duarte Ferreira <sup>8</sup> and Elaine Cristina Paris <sup>2,\*</sup>

- <sup>1</sup> Department of Chemistry, Federal University of São Carlos, São Carlos 13565-905, Brazil; leticiaflschildt@gmail.com (L.F.L.S.); mariasierra@estudante.ufscar.br (M.L.L.S.e.S.); vannylavasconcelos@gmail.com (V.V.V.V.)
- <sup>2</sup> Nanotechnology National Laboratory for Agriculture (LNNA), Embrapa Instrumentação, São Carlos 13560-970, Brazil
- <sup>3</sup> Department of Applied Science and Technology (DISAT), Polytechnic of Turin, Corso Castellidardo 39, 10129 Turin, Italy; corrado.diconzo@polito.it
- <sup>4</sup> Department of Basic and Applied Science for Engineering, Sapienza University of Rome, Via Antonio Scarpa 14, 00161 Rome, Italy; francesco.mura@uniroma1.it (F.M.); marco.rossi@uniroma1.it (M.R.)
- <sup>5</sup> CNR, Istituto di Struttura della Materia, nM2-Lab, Monterotondo Scalo, 00015 Roma, Italy; gaspare.varvaro@cnr.it (G.V.); meryabdolrahimi@gmail.com (M.A.)
- <sup>6</sup> nM2-Lab, Dipartimento di Chimica e Chimica Industriale, Università degli Studi di Genova, Via Dodecaneso 31, 16146 Genova, Italy
- <sup>7</sup> Institute for the Study of Nanostructured Materials, Italian National Research Council (ISMN–CNR), Strada Provinciale 35/d n. 9, Montelibretti, 00010 Rome, Italy; simone.quaranta@cnr.it
- <sup>8</sup> Laboratory of Analysis and Water Treatment, Department of Chemistry, Federal University of Espírito Santo, Vitória 29075-910, Brazil; sandraufes@gmail.com
- \* Correspondence: tainararamos25@gmail.com (T.R.N.); elaine.paris@embrapa.br (E.C.P.)



**Citation:** Neves, T.R.; Schildt, L.F.L.; Silva, M.L.L.S.e.; Vasconcelos, V.V.V.; Di Conzo, C.; Mura, F.; Rossi, M.; Varvaro, G.; Abdolrahimi, M.; Quaranta, S.; et al. Magnetic CuFe<sub>2</sub>O<sub>4</sub> Nanoparticles Immobilized on Modified Rice Husk-Derived Zeolite for Chlorogenic Acid Adsorption. *Magnetochemistry* **2024**, *10*, 87. <https://doi.org/10.3390/magnetochemistry10110087>

Academic Editor: Wei Ding

Received: 10 July 2024

Revised: 26 October 2024

Accepted: 30 October 2024

Published: 4 November 2024



**Copyright:** © 2024 by the authors. Licensee MDPI, Basel, Switzerland. This article is an open access article distributed under the terms and conditions of the Creative Commons Attribution (CC BY) license (<https://creativecommons.org/licenses/by/4.0/>).

**Abstract:** Adsorption has emerged as a promising method for removing polyphenols in water remediation. This work explores chlorogenic acid (CGA) adsorption on zeolite-based magnetic nanocomposites synthesized from rice husk waste. In particular, enhanced adsorbing materials were attained using a hydrothermal zeolite precursor (Z18) synthesized from rice husk and possessing a remarkable specific surface area (217.69 m<sup>2</sup> g<sup>-1</sup>). A composite material was prepared by immobilizing magnetic copper ferrite on Z18 (Z18:CuFe<sub>2</sub>O<sub>4</sub>) to recover the zeolite adsorbent. In addition, Z18 was modified (Z18 M) with a mixture of 3-aminopropyltriethoxysilane (APTES) and trimethylchlorosilane (TMCS) to improve the affinity towards organic compounds in the final nanocomposite system (Z18 M:CuFe<sub>2</sub>O<sub>4</sub>). While the unmodified composite demonstrated inconsequential CGA removal rates, Z18 M:CuFe<sub>2</sub>O<sub>4</sub> could adsorb 89.35% of CGA within the first hour of operation. Z18 M:CuFe<sub>2</sub>O<sub>4</sub> showed no toxicity for seed germination and achieved a mass recovery of 85% (due to a saturation magnetization of 4.1 emu g<sup>-1</sup>) when an external magnetic field was applied. These results suggest that adsorbing magnetic nanocomposites are amenable to CGA polyphenol removal from wastewater. Furthermore, the reuse, revalorization, and conversion into value-added materials of agro-industrial waste may allow the opportunity to implement sustainability and work towards a circular economy.

**Keywords:** wastewater; chlorogenic acid; adsorption; magnetic nanocomposite; zeolite; rice husk

## 1. Introduction

Over the last few decades, the disposal of wastewater generated by the food industry has become a significant environmental concern. Industries such as the wine, coffee, and olive oil industries produce large volumes of wastewater with an acidic pH and high levels of organic pollutants, especially polyphenols (PPs). These PPs may negatively impact

ecological systems [1,2] since their antimicrobial characteristics make them unsusceptible to biological degradation. Hence, applying contaminated water with PPs in irrigation systems or disposal into watercourses can unbalance ecosystems. In addition, polyphenols may be toxic to vegetables and other live organisms [2–4]. Thus, treating wastewater containing high amounts of PPs has become a significant challenge for water remediation and the environment. Global organizations such as the US Environmental Protection Agency (EPA), European Union (EU) and the World Health Organization (WHO) listed phenolic compounds as priority pollutants to be removed. These agencies recommend a maximum PP concentration of  $1 \text{ mg L}^{-1}$  in wastewater and less than  $0.001 \text{ mg L}^{-1}$  in drinking water [5].

The 5-O-caffeoylquinic acid, CGA, belongs to the polyphenol family and is widely encountered in various plant-based foods, such as grapes, coffee, and apples [6]. CGA possesses anti-inflammatory and anticarcinogenic properties [7,8] that make this compound and its isomers potentially useful for application in pharmaceuticals, food products [9], and cosmetics [10,11]. In particular, waste stemming from the artichoke [12], coffee [13], olives, and wine [14] processing industries (produced in droves every year) contains large CGA amounts. Hence, CGA removal and recovery for reuse from contaminated wastewater positively contribute to the circular economy perspective. In this context, the adsorption process is a methodology that contributes to this view since it allows the removal and recovery of PPs, such as CGA, without molecule degradation in byproducts.

Adsorption with inexpensive materials is considered an essential tool for environmental remediation. It can be regarded as one of the most efficient and economical techniques to effectively remove both inorganic and organic pollutants from industrial wastewater [15,16]. The zeolite family stands out among the different adsorbent types due to their high surface area, regular pore size distribution, ion exchange capacity, and selectivity [17]. In particular, faujasite (FAU) zeolite possesses a high pore diameter, around  $7.4 \text{ \AA}$  [18], which favors the adsorption of organic compounds. Naturally, investigating new methods for obtaining zeolites from industrial residues is a plausible way to accomplish a circular economy and sustainability by reusing low-value raw materials to produce high-performing adsorbents. Consequently, the green synthesis of various zeolite types from residues, such as agribusiness, has been constantly studied [19,20]. Rice husk waste contains around 15 to 20% silica by mass [21] and is an excellent raw material for zeolite production.

Rice is the second most produced cereal in the world, and the current rice husk disposal rate has reached roughly 120 million tons annually [22]. Inadequate management of rice husks, such as landfilling or open burning, causes serious environmental issues. Rice husk can be used as a  $\text{SiO}_2$  source, being a candidate to contribute to commercial silica supply from agribusiness waste [23–25]. Chat et al. (2022) [26] synthesized zeolite X by taking advantage of silica extracted from rice husks for the adsorption of propionic acid. In this study, the authors obtained a silica yield of 23.43%, corresponding to a purity of 81.36% ( $w w^{-1}$ ). The zeolitic material had a specific surface area of  $543.3 \text{ m}^2 \text{ g}^{-1}$ , resulting in an adsorption capacity of  $516 \text{ mg g}^{-1}$  concerning propionic acid. In addition, the surface of zeolite particles can be modified to promote interaction with organic molecules [27]. In this sense, surfactants and organosilanes are remarkably effective in functionalizing zeolites [28–30]. Hashemi et al. (2019) [31] investigated the adsorption capacity of zeolite synthesized from natural bentonite in conjunction with cetrimonium bromide (CTAB) modification to remove contaminants from industrial effluents. The adsorption process achieved an 89% removal rate of organic pollutants, with an adsorption capacity of  $30.87 \text{ mg g}^{-1}$ .

However, particulate adsorbent recovery from the aqueous medium is still a challenge. This fact can make pollutant removal by adsorption unpractical, if not unfeasible. In particular, obtaining a magnetic nanocomposite system from ferrites has already been applied to wastewater treatment, which is becoming a promising approach.

Copper ferrite ( $\text{CuFe}_2\text{O}_4$ ) is highlighted among different ferrite types due to its thermal stability and unique magnetic properties [32]. The spinel structure enhances these magnetic characteristics, making the  $\text{CuFe}_2\text{O}_4$  ideal for magnetic applications [33]. It exhibits excel-

lent catalytic activity and adsorption capabilities, facilitating efficient pollutant removal from wastewater and acting as a catalyst in various chemical reactions [34]. In addition to its adsorbent properties, copper ferrite has a wide range of applications, including magnetic sensors and inductors [33], biosensors for detecting biomolecules and pathogens [35], and energy storage in lithium-ion batteries [36] and solar devices [37].

The effective response to the magnetic field of the copper ferrite can also enhance the combination of this advanced material with different types of particulate porous adsorbents, such as zeolites, favoring magnetic removal after the process. Kharazi et al. (2019) [38] synthesized a magnetic nanocomposite comprising copper ferrite and polyaniline for the adsorption of methyl orange dye. The composite had a mesoporous structure, a surface area of  $20.37 \text{ m}^2 \text{ g}^{-1}$  with an adequate adsorption capacity of  $345.9 \text{ mg g}^{-1}$ , and magnetic properties that enabled it to be easily separated through an external magnetic field.

This work aimed to incorporate copper ferrite nanoparticles on the surface of zeolite synthesized from rice husk waste (primary adsorbent material) to guarantee the recovery of the resulting magnetic nanocomposite (zeolite: $\text{CuFe}_2\text{O}_4$ ) by applying an external magnetic field. To the best of our knowledge, this is the first paper about the CGA adsorption of waste-derived zeolite synthesized from rice husks. The present work reuses agribusiness waste and proposes a new generation of smart adsorbents for wastewater decontamination. This route would minimize waste generation and sustain wastewater reuse or proper disposal. Although this research used a standard CGA source, the obtained system (zeolite: $\text{CuFe}_2\text{O}_4$ ) is a promising material for future applications in real industrial wastewater due to effective environmental remediation technology.

## 2. Materials and Methods

### 2.1. Materials

Rice husk, as a grain manufacturing byproduct, was supplied by the rice processing company Máquina Popular (Aparecida do Taboado-MS, Brazil). Sodium Aluminate ( $\text{NaAlO}_2$ , 98%), Copper Nitrate [ $\text{Cu}(\text{NO}_3)_2$ , 98%], TMCS ( $\text{C}_3\text{H}_9\text{SiCl}$ ,  $\geq 99\%$ ), APTES ( $\text{C}_9\text{H}_{23}\text{NO}_3\text{Si}$ ,  $\geq 99\%$ ), CGA ( $\text{C}_{16}\text{H}_{18}\text{O}_9$ , 99.8%) were obtained from Sigma-Aldrich (St. Louis, MO, USA). Sodium Hydroxide ( $\text{NaOH}$ , 97%) and Iron Nitrate [ $\text{Fe}(\text{NO}_3)_3$ , 98%] were purchased from Synth (Brazil). Hydrochloric Acid ( $\text{HCl}$ , 37%) and Ethyl Alcohol ( $\text{C}_2\text{H}_6\text{O}$ , 99.5%) were attained from Vetec (Brazil). All reagents were used as received. Decarbonized, deionized water ( $\rho = 18.2 \text{ M}\Omega \text{ cm}$ ) purified through the Milli-Q system (Bamstead Nanopure Diamond, Thermo Fisher Scientific Inc., Waltham, MA, USA) was used in all procedures.

### 2.2. $\text{SiO}_2$ Extraction from Rice Husks

High-purity silica ( $\text{SiO}_2$ ) to be used in the sustainable synthesis of zeolite was prepared from rice husk through the methodology described in Malafatti et al. (2023) [39]. Briefly, to eliminate metallic impurities (e.g., Fe, alkali, and alkali-earth metals), 10 g of rice husks were immersed in 200 mL of aqueous  $\text{HCl}$  solution ( $3 \text{ mol L}^{-1}$ ) for 3 h, under magnetic stirring. The rice husks were then separated from the acid solution by filtration and washed up to pH neutrality. Samples were dried in a circulation oven at  $60 \text{ }^\circ\text{C}$  for 24 h and then subjected to two consecutive heat treatments at  $300 \text{ }^\circ\text{C}$  and  $600 \text{ }^\circ\text{C}$ , both for 3 h, to eliminate the organic components of the material.

### 2.3. Zeolite Synthesis

The zeolite was synthesized by adapting the procedure reported in Meirelles et al. (2023) [17]. In particular, silica extracted from rice husks replaced commercial  $\text{SiO}_2$ . Initially, sodium aluminate was solubilized in deionized water under magnetic stirring until a translucent solution was obtained. Subsequently, a  $2.9 \text{ mol L}^{-1}$  sodium hydroxide aqueous solution was added. After homogenization, the silica from rice husks was incorporated into the mixture under vigorous stirring to attain a homogeneous gel. After 24 h of static aging, the gel was hydrothermally treated at  $100 \text{ }^\circ\text{C}$  for 18 h under magnetic stirring. The

final product was repeatedly washed by centrifugation until  $\text{pH} \leq 8$ . Finally, the solid was dried in a circulation oven at  $60\text{ }^\circ\text{C}$  for 24 h and deagglomerated. The attained zeolite sample was labeled as Z18.

#### 2.4. Zeolite Modification with Silane Agents

The Z18 sample was modified with silane agents (APTES and TMCS) to facilitate the interaction between the hydrophilic zeolite and the organic contaminant during the adsorption tests [30,40]. APTES and TMCS were combined in a 1:1 ( $\text{V V}^{-1}$ ) ratio. Thus, 0.5 g of zeolite was suspended with 0.5 mL of each modifier in 10 mL of a 3-to-1 ethanol–water mixture in a 250 mL flask. The system was refluxed under magnetic stirring at  $100\text{ }^\circ\text{C}$  for 24 h. The material obtained after modification was washed, dried in an oven at  $60\text{ }^\circ\text{C}$ , and identified as Z18 M.

#### 2.5. Synthesis of Copper Ferrite

Copper ferrite ( $\text{CuFe}_2\text{O}_4$ ) was prepared for the coprecipitation method according to the methodology proposed by Paris et al. (2020) [16]. Two aqueous solutions of equal volumes of iron (III) nitrate  $0.40\text{ mol L}^{-1}$  and copper nitrate  $0.20\text{ mol L}^{-1}$  were mixed under magnetic stirring for 15 min. An aqueous  $\text{NaOH}$   $3.0\text{ mol L}^{-1}$  solution was added drop by drop (always under stirring). After completing the hydroxide addition, the copper ferrite precursor was left under magnetic stirring for 30 min. The material was then washed by centrifugation to reach  $\text{pH} \leq 8$ . The solid was dried in a circulation oven at  $60\text{ }^\circ\text{C}$  for 24 h and submitted to consecutive heat treatment at  $300\text{ }^\circ\text{C}$  for 4 h and  $500\text{ }^\circ\text{C}$  for 3 h.

#### 2.6. Zeolite: $\text{CuFe}_2\text{O}_4$ Magnetic Nanocomposites

The magnetic nanocomposites with copper ferrite were synthesized from both pure (Z18) and modified (Z18 M) zeolites, according to studies published in the literature [16,17]. Briefly, 0.1 g of copper ferrite was suspended in 40 mL of distilled water by ultrasonication (60% amplitude) for 20 min in an ice bath. Once the ferrite was dispersed entirely, 0.3 g of zeolite was gradually added to the suspension until the zeolite: $\text{CuFe}_2\text{O}_4$  ratio reached 3:1 ( $\text{m m}^{-1}$ ). The process was assisted by sonication for 50 min to ensure composite homogenization. Finally, the material was dried in an oven at  $60\text{ }^\circ\text{C}$  for 24 h for characterization and application in the adsorption tests. The prepared materials were named Z18: $\text{CuFe}_2\text{O}_4$  and Z18 M: $\text{CuFe}_2\text{O}_4$ , for the pristine and modified zeolite, respectively.

#### 2.7. Characterizations

X-ray diffraction (XRD) measurements were performed using a Shimadzu XRD 6000 diffractometer with Ni-filter  $\text{Cu-K}\alpha$  radiation ( $\lambda = 1.5405\text{ \AA}$ ) in the  $5\text{--}80^\circ$   $2\theta$  range (scan rate  $1^\circ\text{ min}^{-1}$ ). Low angle ( $0\text{--}10^\circ$ ) XRD scans were performed with a Rigaku SmartLab diffractometer equipped with a knife-edge slit. Field Emission Scanning Electron Microscopy (SEM-FEG) measurements were conducted with a JEOL microscope model JSM-6701F running at 5 kV. X-ray dispersive energy spectroscopy (EDS) JEOL-JSM 6510 at 15 kV was used to evaluate the purity of silica extracted from rice husks and the magnetic nanocomposite. Transmission Electron Microscope (TEM) analysis was performed with a JEOL JEM F200, operating at 200kV and equipped with an Energy-Dispersive X-ray Spectrometer.  $\text{N}_2$  adsorption/desorption curves were collected using Micromeritics ASAP 200 surface analysis equipment. The Brunauer, Emmett, and Teller (BET) method extrapolated specific surface areas. In contrast, the Barrett–Joyner–Hallenda model was used to determine the pore size distribution. Thermal degradation of samples was carried out in platinum crucibles using a TGA Q500 thermo-analyzer, TA Instruments. Samples (approximately 5 mg) were heated from RT to  $900\text{ }^\circ\text{C}$  with a heating rate of  $10\text{ }^\circ\text{C min}^{-1}$  under synthetic air ( $60\text{ mL min}^{-1}$ ). Zeta Potential measurements were performed using a Zetasizer Nano ZS90, Malvern Instruments, using 4 mg of particles/20 mL Milli-Q water. Magnetization vs. applied field measurements were performed at  $26.85\text{ }^\circ\text{C}$  using a vibrating sample magnetometer (VSM Model 10—MicroSense) equipped with an electromagnet and a pick-up coil



system to detect the moment. Powder samples were placed within polycarbonate capsules (a few mg) and immobilized with epoxy resin to prevent any displacements during the measurements.

### 2.8. CGA Adsorption Tests

CGA UV-Vis spectrum has been considered pH-sensitive [41]. Hence, an investigation concerning CGA optical absorbance dependence on pH (with a CGA concentration equal to  $20 \text{ mg L}^{-1}$ ) was carried out before the adsorption experiments. pH was adjusted over the 3–12 range by using NaOH and HNO<sub>3</sub> solutions. CGA adsorption was performed under the following experimental conditions: 10 mL of aqueous CGA solution was added to Falcon® tubes containing 20 mg ( $2 \text{ g L}^{-1}$ ) of magnetic nanocomposites. The experiments were conducted in triplicates under mechanical agitation (150 rpm) for 1, 3, 6, 12, 24, 36, and 48 h. After removing the adsorbents, the aliquots were analyzed using UV-Vis spectrophotometry (UV-1601PC Shimadzu, Kyoto, Japan UV-1601PC) in the 200 to 450 nm region. CGA removal rate (%) was calculated (from the maximum UV-Vis absorbance) according to Equation (1).

$$\text{Removalrate\%} = \frac{(C_t - C_i)}{C_i} \times 100 \quad (1)$$

where  $C_i$  ( $\text{mg L}^{-1}$ ) is the initial polyphenol concentration, and  $C_t$  ( $\text{mg L}^{-1}$ ) is the concentration at time  $t$  (min). CGA adsorption kinetics was evaluated by applying the pseudo-first-order and pseudo-second-order models according to the following equations:

Pseudo-first-order:

$$\log(q_e - q_t) = \log q_e - \frac{k_1}{2.303} t \quad (2)$$

Pseudo-second-order:

$$\frac{t}{q_t} = \frac{1}{k_2 q_e^2} + \frac{1}{q_e} t \quad (3)$$

where  $q_e$  ( $\text{mg g}^{-1}$ ) is the amount of CGA adsorbed (i.e., adsorption capacity) at equilibrium and  $q_t$  ( $\text{mg g}^{-1}$ ) is the amount adsorbed at time  $t$  (min). The rate constants for the pseudo-first- and pseudo-second-order reactions are represented by  $k_1$  ( $\text{min}^{-1}$ ) and  $k_2$  ( $\text{g mg}^{-1} \text{min}^{-1}$ ), respectively. The nanocomposite with the highest CGA adsorption capacity was also tested for germination and mass recovery efficiency.

### 2.9. Germination Test

Nanoparticle germination on living effects can be considered a significant liability for environmental remediation. Therefore, the germination of lettuce seeds (*Lactuca sativa*) was employed as a proxy. Experiments were performed under the same conditions as the adsorption tests. Twenty seeds were placed in contact with the magnetic composite in Falcon® tubes containing distilled water for 1 h at room temperature [42]. A control sample (i.e., blank) containing no composite nanoparticles was also tested for reference. After exposure, the seeds were separated from the aqueous medium and placed in Petri dishes with filter paper. They germinated for 5 days (under natural light). When the roots emerged, microscopic analysis was conducted to assess the effects of nanocomposites on root development.

### 2.10. Magnetic Mass Recovery

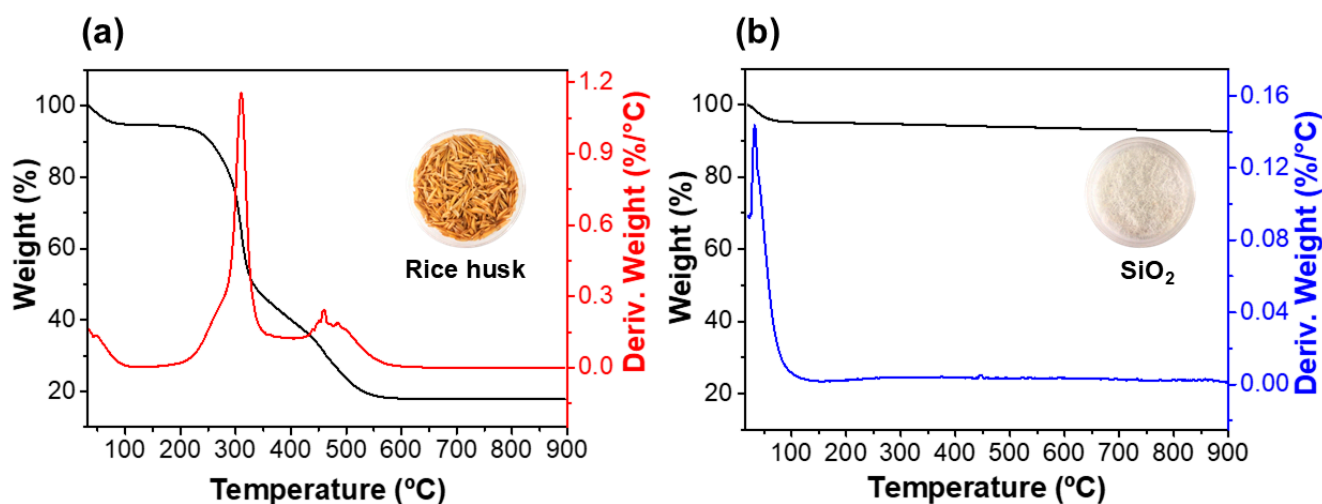
As for the adsorbent mass recovery experiment, approximately 30 mg of the magnetic nanocomposite was weighed. The material was then dispersed in distilled water and subjected to a magnetic field using a cube-shaped neodymium magnet ( $50.8 \text{ mm} \times 50.8 \text{ mm} \times 25.4 \text{ mm}$ ), model N52, with magnetic field strength  $\sim 14,800$  Gauss. After 10 min, the supernatant was carefully discarded, and the material retained by the magnetic field was dried in a circulation oven at  $60 \text{ }^\circ\text{C}$  until constant weight was reached. After drying, the nanocom-

posite was weighed to determine the magnetic recovered mass. Each test was carried out in triplicate over 3 consecutive cycles, and the mass recovery efficiency was determined using Equation (4).

$$\text{Mass recovery (\%)} = \frac{\text{Recovered mass}}{\text{Initial mass}} \times 100 \quad (4)$$

### 3. Results

The thermal analysis (thermogravimetric) measurements of rice husk starting material and silica derived from rice husk are reported in Figure 1. The agricultural residue (Figure 1a) showed a significant mass loss below 100 °C, indicating the release of physisorbed water. A second thermal event, corresponding to lignin and cellulose combustion, was identified at around 330 °C [39]. In addition, the sample presented a weight loss above 400 °C, possibly due to the complete pyrolysis of the organic compounds [43]. The total mass loss amounted to 81.97%, following the amount of inorganic compounds usually encountered in rice husk. In contrast, SiO<sub>2</sub> (Figure 1b) revealed a progressive mass loss of 7.22% over a wide range of temperatures. Aside from physically sorbed water, H<sub>2</sub>O molecules interacting with the silanol groups of the silica matrix (i.e., chemisorption) are also released, leading to surface dehydration (OH loss) [44,45]. Hence, a rice husk annealing temperature of 600 °C can be considered ideal to attain a SiO<sub>2</sub> precursor for zeolite synthesis. Indeed, this temperature assures the complete removal of rice husk organic components while pre-empting extensive particle sintering, which is detrimental to zeolite preparation (i.e., low silica reactivity).

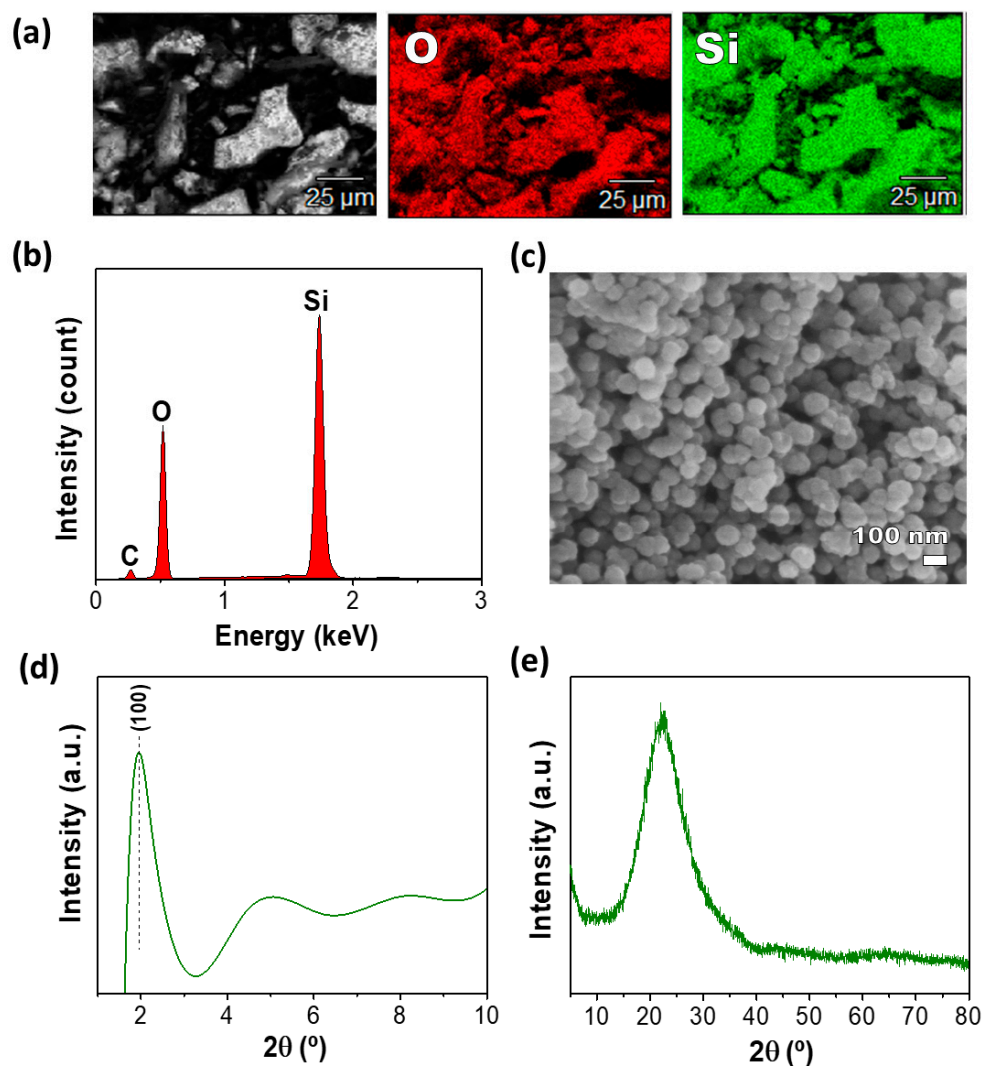


**Figure 1.** TG-DTG of rice husk waste (a) and SiO<sub>2</sub> derived from rice husk (b).

Further studies were conducted to evaluate the silica precursor purity, morphology, and structure (Figure 2). EDS chemical mapping (Figure 2a) showed a homogeneous Si and O distribution. In contrast, the EDS spectrum (Figure 2b) confirmed the predominant presence of silica in the sample. Nonetheless, a small amount of (adventitious) carbon was detected, probably ascribable to the sample handling and preparation procedure for the SEM analysis. EDS analysis could not reveal other impurities, suggesting that the SiO<sub>2</sub> preparation process from rice husk fits the purity and quality requirements of various industrial and technological applications [46].

The SEM-FEG images (Figure 2c) illustrate the presence of agglomerates of rounded-shaped particles with an average diameter varying from 70 to 100 nm. Additionally, the low-angle X-ray diffractogram (Figure 2d) shows an intense peak (100), implying the formation of a mesoporous SiO<sub>2</sub> phase with a hexagonal pore structure [47,48]. The silica X-ray diffraction pattern (Figure 2e) exhibits the typical pattern of an amorphous SiO<sub>2</sub> material with a characteristic broad peak at  $2\theta = 22.2^\circ$  [43,49]. No other phases (like generally highly crystalline metal oxides originating from rice husk impurities) [23]

could be identified, verifying the EDS analysis' findings about the purity of the material. Concerning these results, nanoparticulate silica was obtained from rice husk with a simple acid washing/annealing combination.



**Figure 2.** Analysis of  $\text{SiO}_2$  obtained from rice husk: (a) EDS chemical mapping, (b) EDS spectrum, (c) SEM-FEG image, (d) XRD at low angle, and (e) XRD at conventional angle.

Because of its physical/chemical properties (e.g., particle size, porosity, purity, etc.), the silica recovered from rice husk was used as a precursor in the sustainable synthesis of zeolites. This approach posits replacing commercial silica precursors and bringing about cost reduction and environmental impact mitigation.

The XRD diffractograms of the synthesized zeolite are reported in Figure 3. FAU (JCPDS n° 38-238) and NaP-type GIS (JCPDS n° 89-6322) zeolites were identified. As reported in the literature [50,51], it is not unusual to end up with a GIS-FAU mixture when waste-based Si or Al sources are employed, since the growth of six-(faujasite structure) and four-(gismondine structure)-membered rings are in direct competition. For instance, Maatoug et al. (2018) [52] synthesized zeolitic materials from vitreous waste in China, obtaining a mixture of FAU, NaP, and sodalite (SOD) phases caused by the influence of crystallization time on the structure and morphology of the final zeolite.

Additionally, Figure 3 shows that the modification process with silane agents did not affect the sample structure since the modified zeolite (Z18 M) shows all the diffraction peaks corresponding to the FAU and NaP phases, as in Z18.

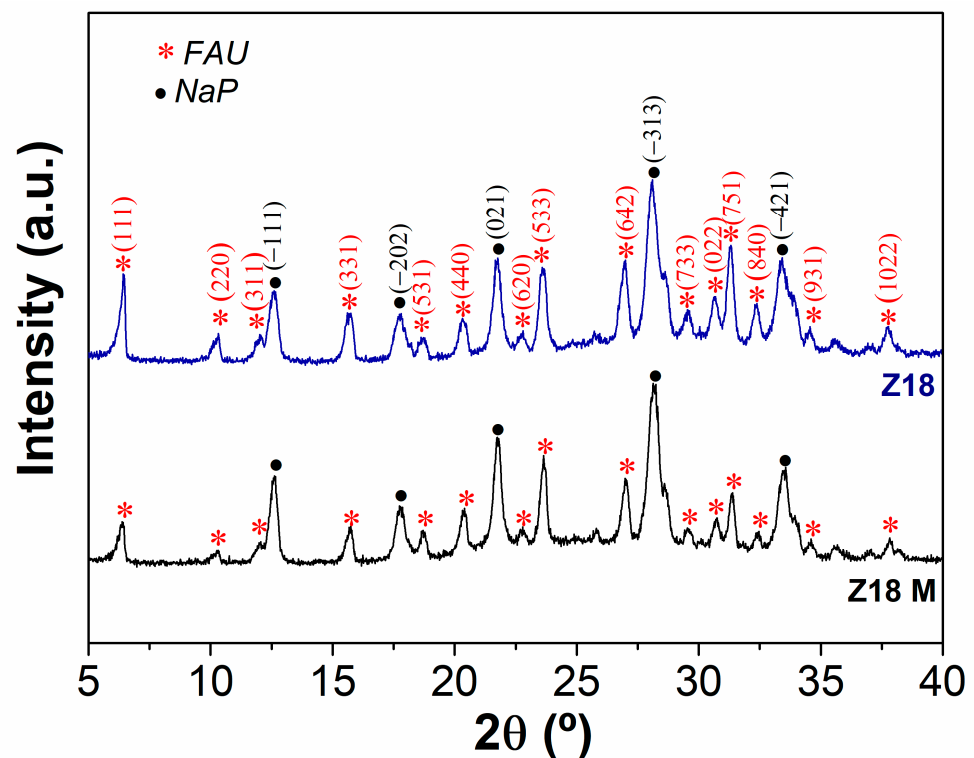


Figure 3. XRD diffractograms of zeolite before (Z18) and after silanization (Z18 M).

Z18 and Z18M samples were also compared in terms of thermal stability. Figure 4 shows the material thermogravimetric curves before and after modification. Both samples present an initial weight loss at approximately 100 °C due to the evaporation of water molecules physically adsorbed on the surface of the zeolites. Then, Na<sup>+</sup> cations hydration water (i.e., H<sub>2</sub>O structural molecules needed to stabilize the zeolite framework) was lost for both samples, up to 300 °C [53,54]. However, Z18 mass loss stabilizes at 300 °C, with a total of 20.31%. By contrast, Z18 M shows an additional mass loss between 300 °C and 600 °C. This loss corresponds to the elimination of organic modifiers (APTES and TMCS), totaling a final mass loss of 23.25%. The difference between the final and zeolite mass loss contributions indicates a degree of surface modification by silane agents of 2.94% (m m<sup>-1</sup>).

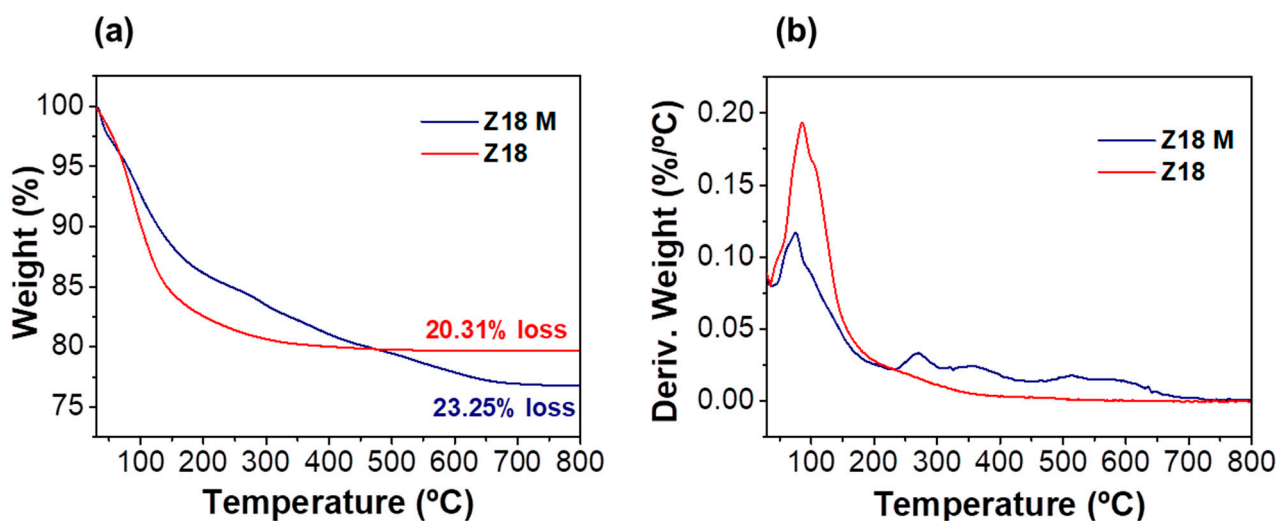
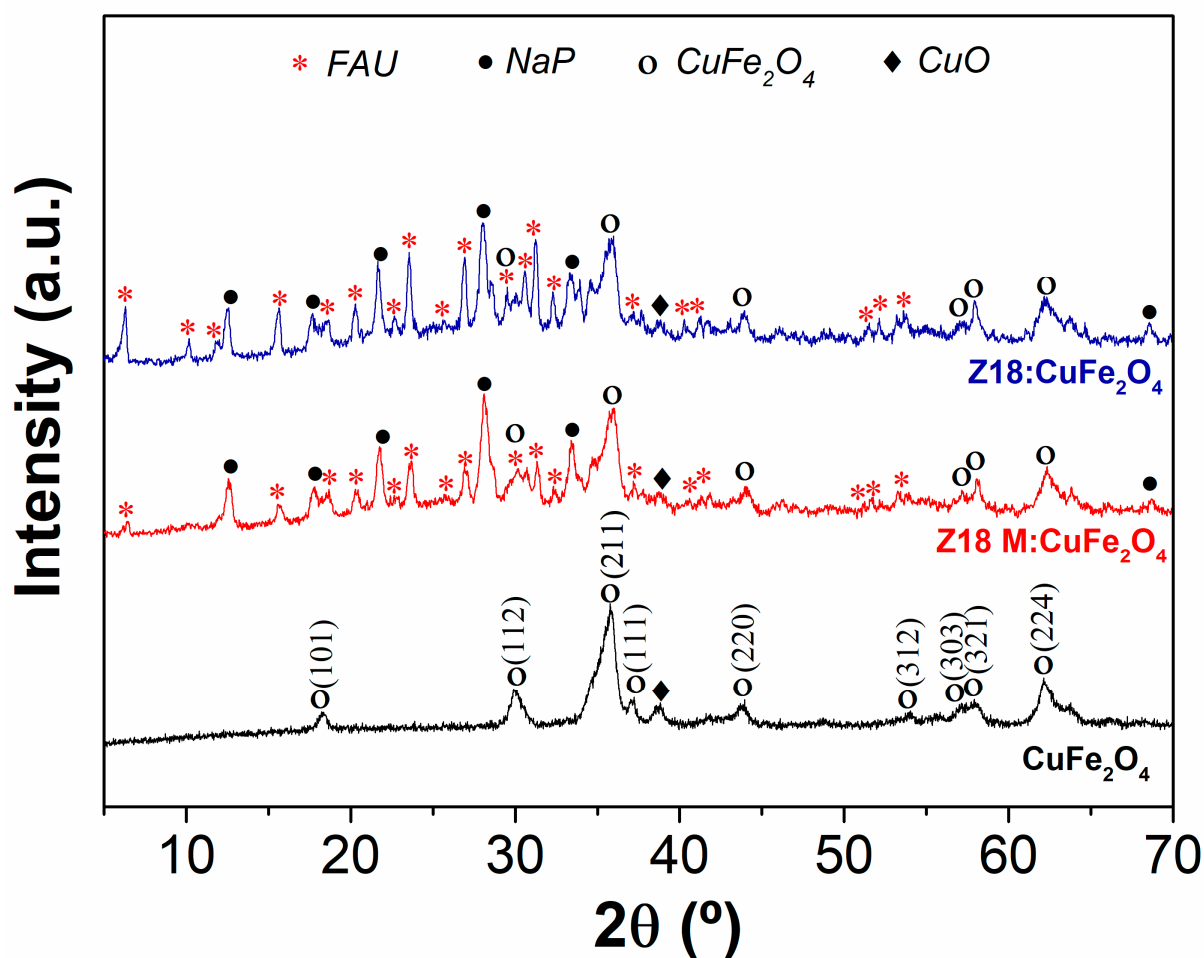


Figure 4. Thermal analysis curves of the Z18 and Z18M samples: (a) Weight loss pattern, (b) derivative weight loss.

Figure 5 shows the XRD patterns of copper ferrite and both composite materials. The ferrite diffractogram reveals the formation of the cubic  $\text{CuFe}_2\text{O}_4$  as a main crystalline phase.  $\text{CuFe}_2\text{O}_4$  reflections could be identified at  $2\theta$  equal to  $19^\circ$ ,  $30^\circ$ ,  $35^\circ$ ,  $36^\circ$ ,  $44^\circ$ ,  $54^\circ$ ,  $56^\circ$ ,  $57^\circ$ , and  $62^\circ$  (JCPDS card n° 34-425). A peak at  $2\theta = 39^\circ$  of  $\text{CuO}$  (JCPDS card n° 45-937) could also be noticed, indicating the presence of this secondary phase. As expected, the Z18 M: $\text{CuFe}_2\text{O}_4$  and Z18: $\text{CuFe}_2\text{O}_4$  diffraction patterns features of  $\text{CuFe}_2\text{O}_4$  and zeolites (NaP and FAU) could be recognized. Therefore, XRD data verified  $\text{CuFe}_2\text{O}_4$  incorporation in the zeolite matrix. As expected, the two zeolite phases were found to be the dominant component of the composite material.



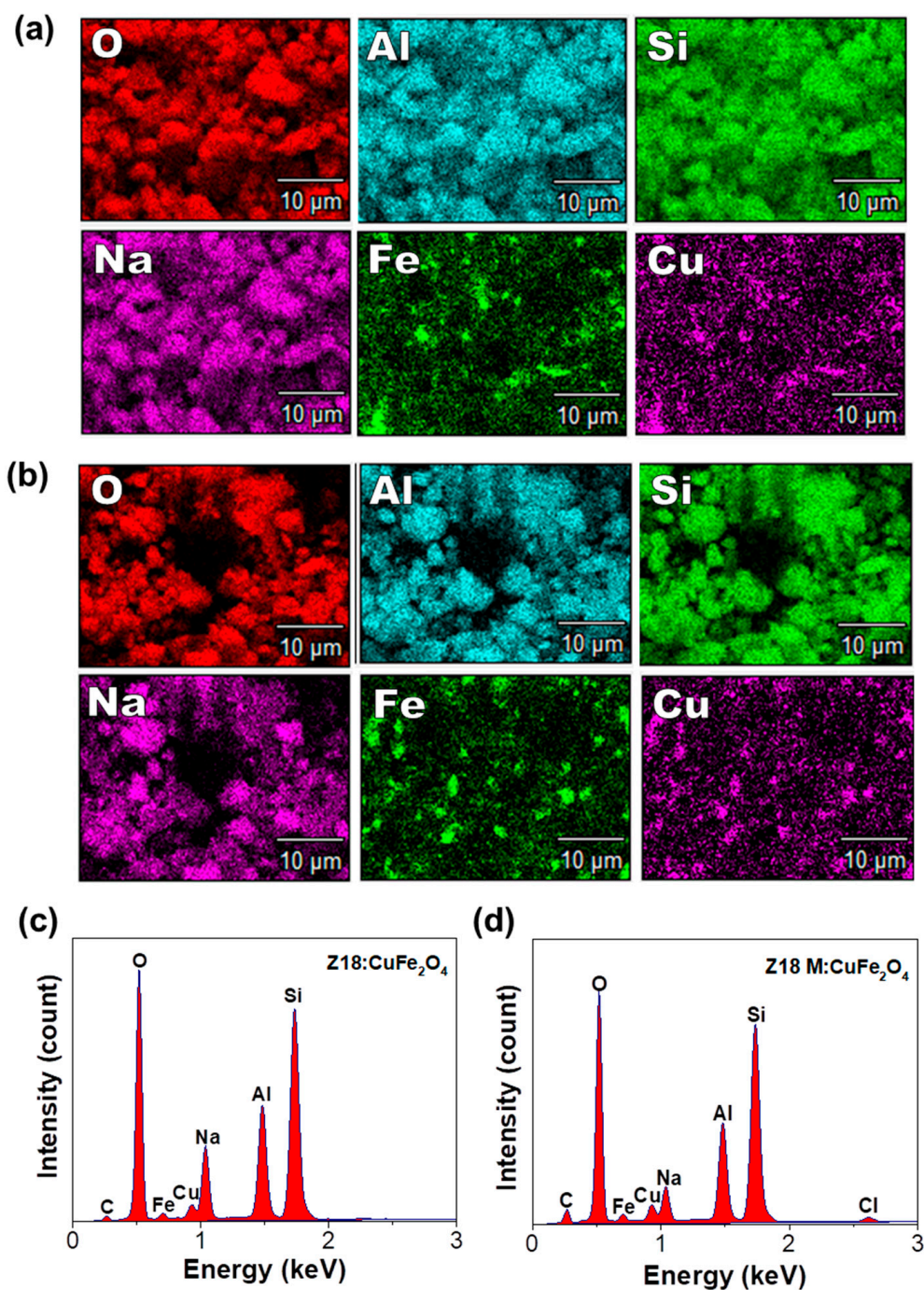
**Figure 5.** XRD patterns of the  $\text{CuFe}_2\text{O}_4$ , Z18 M:  $\text{CuFe}_2\text{O}_4$ , and Z18: $\text{CuFe}_2\text{O}_4$  samples.

The EDS chemical mapping, shown in Figure 6, disclosed the significant incorporation of the copper ferrite into the zeolite matrix, indicating the efficient homogenization of the magnetic and adsorbing components of the composite (Figure 6a,b). The corresponding spectra (Figure 6c,d) indicate the presence of the zeolite elements (O, Si, Al, and Na) and the ferrite (Cu and Fe) elements. Therefore, the zeolite:ferrite ratio 3:1 seems adequate for magnetic material immobilization on the aluminosilicate surface.

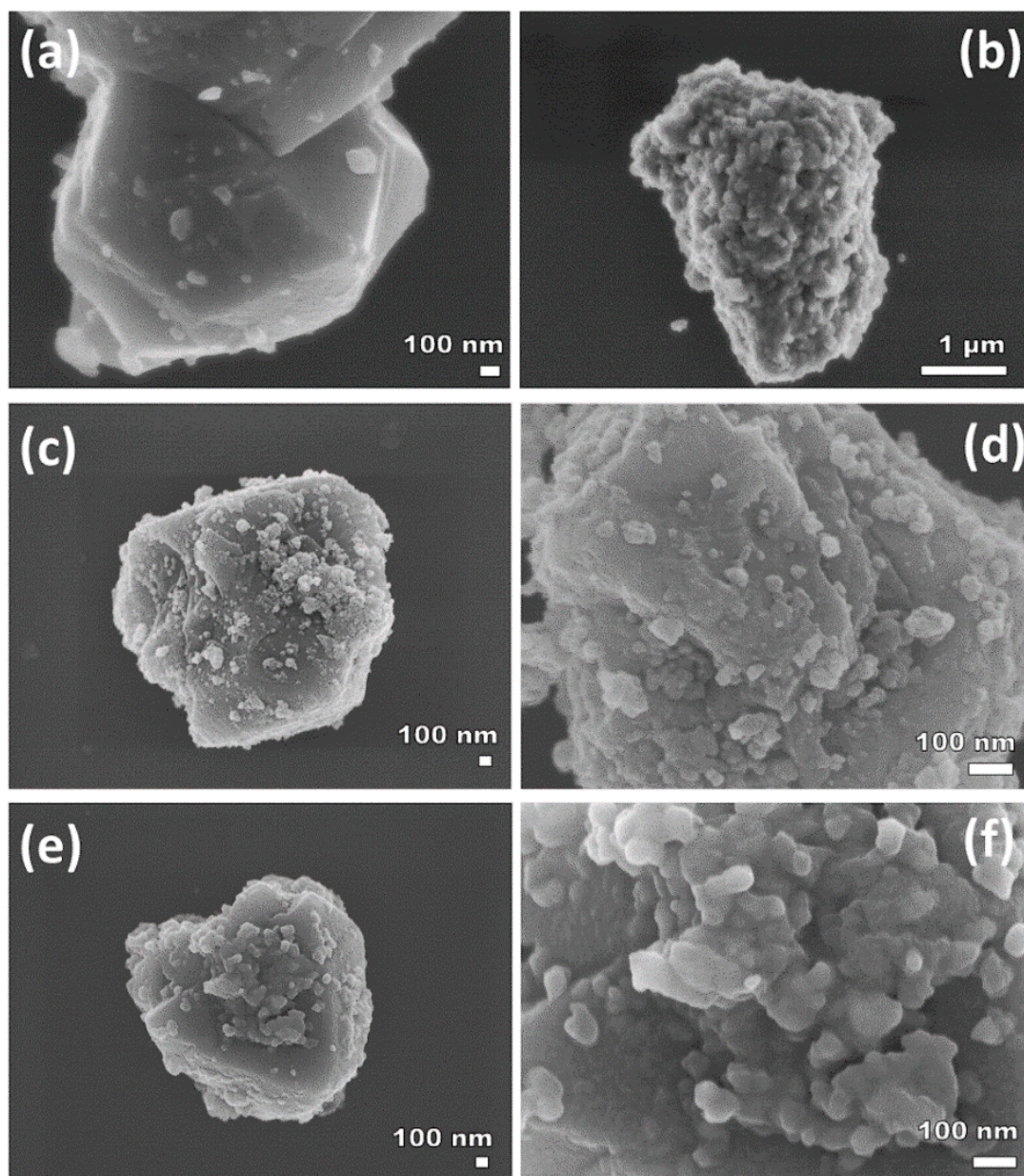
SEM-FEG analysis (Figure 7) was used to investigate the morphology of Z18 zeolite,  $\text{CuFe}_2\text{O}_4$ , and composite samples (Z18: $\text{CuFe}_2\text{O}_4$  and Z18 M: $\text{CuFe}_2\text{O}_4$ ). It can be noticed that the Z18 sample has a diameter in the range of  $(1.43 \pm 0.50) \mu\text{m}$  (Figure 7a), with a characteristic faceted octahedral shape, typical of a well-defined FAU zeolite morphology [55,56]. The copper ferrite presents a smaller particle size, with an average diameter of  $(43.9 \pm 9.40) \text{nm}$  (Figures 7b and 8c), showing a relevant agglomeration level. This effect can probably be ascribed to the intermolecular and magnetic interactions between



particles, which is already expected for ferrites with a spinel structure [57]. Despite agglomeration, ferrite nanoparticles were well distributed over the Z18 surface (Figure 7c,d). It is worth noticing that surface modification with silane agents did not affect the morphology and, consequently, zeolite modification with the ferrite (Figure 7e,f). In the work by Meirelles et al. (2023) [17], a FAU:MgFe<sub>2</sub>O<sub>4</sub> (3:1) nanocomposite was synthesized by the sonication method. The authors observed smaller, agglomerated particles on the faujasite surface. These findings are compatible with magnesium ferrite nanoparticles anchored on the zeolite surface because of the dipolar interactions between the magnetic phases.



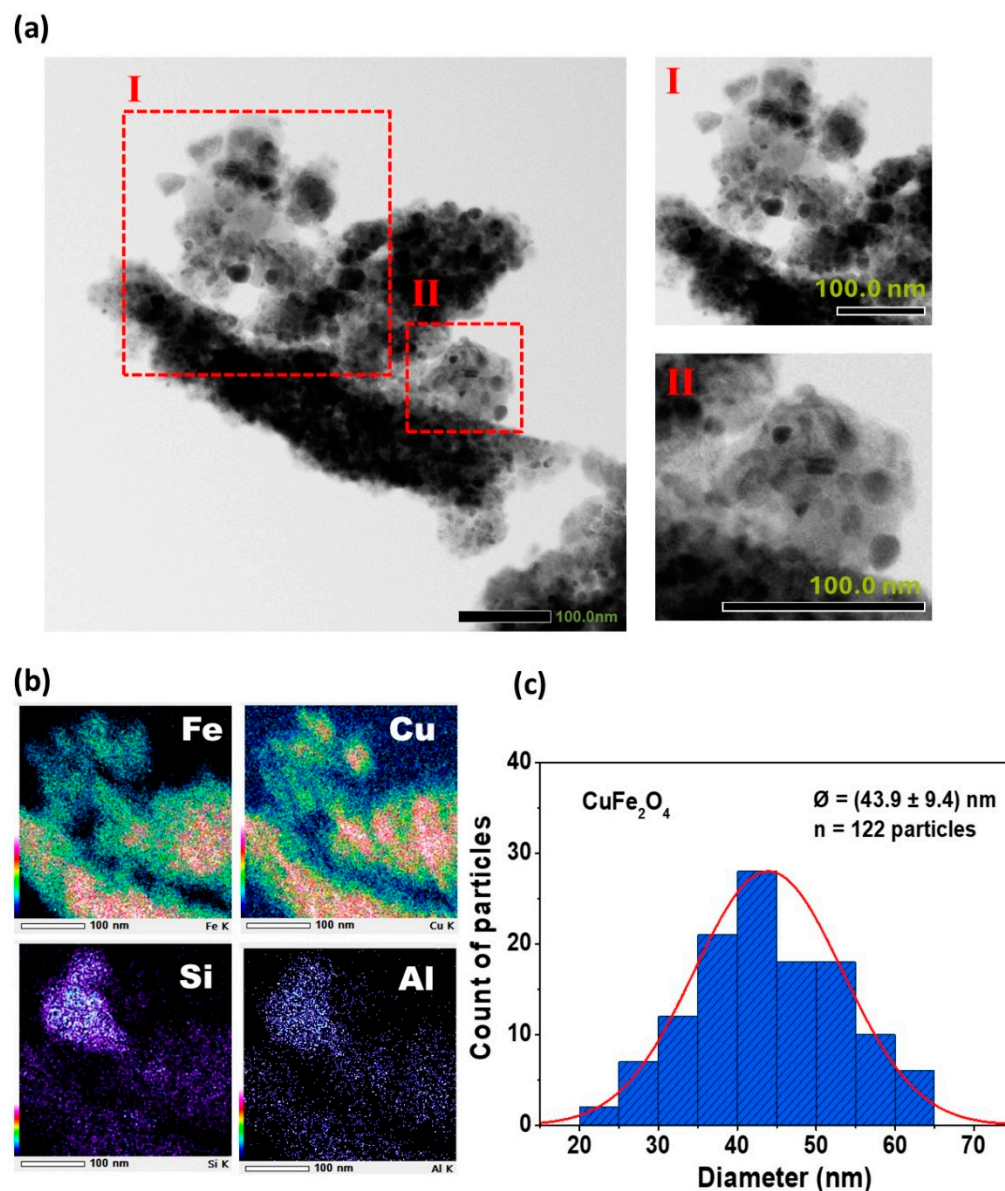
**Figure 6.** EDS analysis. Chemical mapping: (a) Z18:CuFe<sub>2</sub>O<sub>4</sub> and (b) Z18 M:CuFe<sub>2</sub>O<sub>4</sub>; spectrum: (c) Z18:CuFe<sub>2</sub>O<sub>4</sub> and (d) Z18 M:CuFe<sub>2</sub>O<sub>4</sub>.



**Figure 7.** SEM-FEG for samples: (a) Z18, (b) CuFe<sub>2</sub>O<sub>4</sub>, (c,d) Z18:CuFe<sub>2</sub>O<sub>4</sub>, and (e,f) Z18 M:CuFe<sub>2</sub>O<sub>4</sub>.

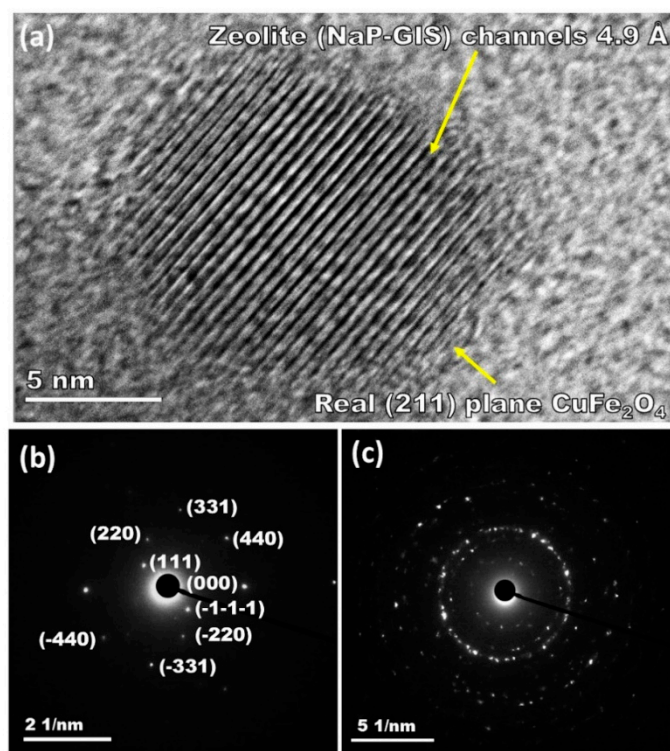
To complement the results obtained by SEM-EDS, TEM analyses of the composite were carried out, including an EDS mapping of the region and the histogram of the size distribution of the ferrite particles, as shown in Figure 8. The analysis indicates agglomeration of the ferrite nanoparticles on the surface of the zeolitic material, which aligns with the SEM-FEG images. Despite the agglomeration, the nanoparticles are dispersed in the structure of the adsorbent, as evidenced by EDS in region I (Figure 8a,b). Furthermore, an analysis of the particle size distribution (Figure 8c) revealed that the average diameter of the copper ferrite particles is in the nanometric range from 20 to 65 nm, confirming their nanostructured characteristics.





**Figure 8.** Analyses of nanocomposite and ferrite: (a) TEM Z18:CuFe<sub>2</sub>O<sub>4</sub>; (b) EDS Z18:CuFe<sub>2</sub>O<sub>4</sub>; and (c) CuFe<sub>2</sub>O<sub>4</sub> diameter histogram of the particle sizes.

TEM images are reported in Figure 9, together with electron diffraction reciprocal space patterns. Figure 9a shows the Z18:CuFe<sub>2</sub>O<sub>4</sub> structural features. In particular, NaP-GIS 4.9 Å-wide channels are visible. Furthermore, copper ferrite (211) planes (most intense CuFe<sub>2</sub>O<sub>4</sub> diffraction signal, see Figure 5) were identified in the composite material. The FAU electron diffraction pattern in the Z18 sample is reported in Figure 9b. FAU (111), (220), (331), and (440) planes can be appreciated, agreeing with the X-ray diffraction Miller indices for the FAU zeolite (Figure 3). Conversely, the composite material electron diffraction pattern is polycrystalline (i.e., not well-defined diffraction spots) and can be regarded as a combination of zeolite and ferrite materials (Figure 9c). The TEM findings verify the XRD results. In fact, the Z18 sample is confirmed to comprise both NaP-GIS and FAU zeolites, whereas Z18:CuFe<sub>2</sub>O<sub>4</sub> possesses both zeolite phases and ferrite components.

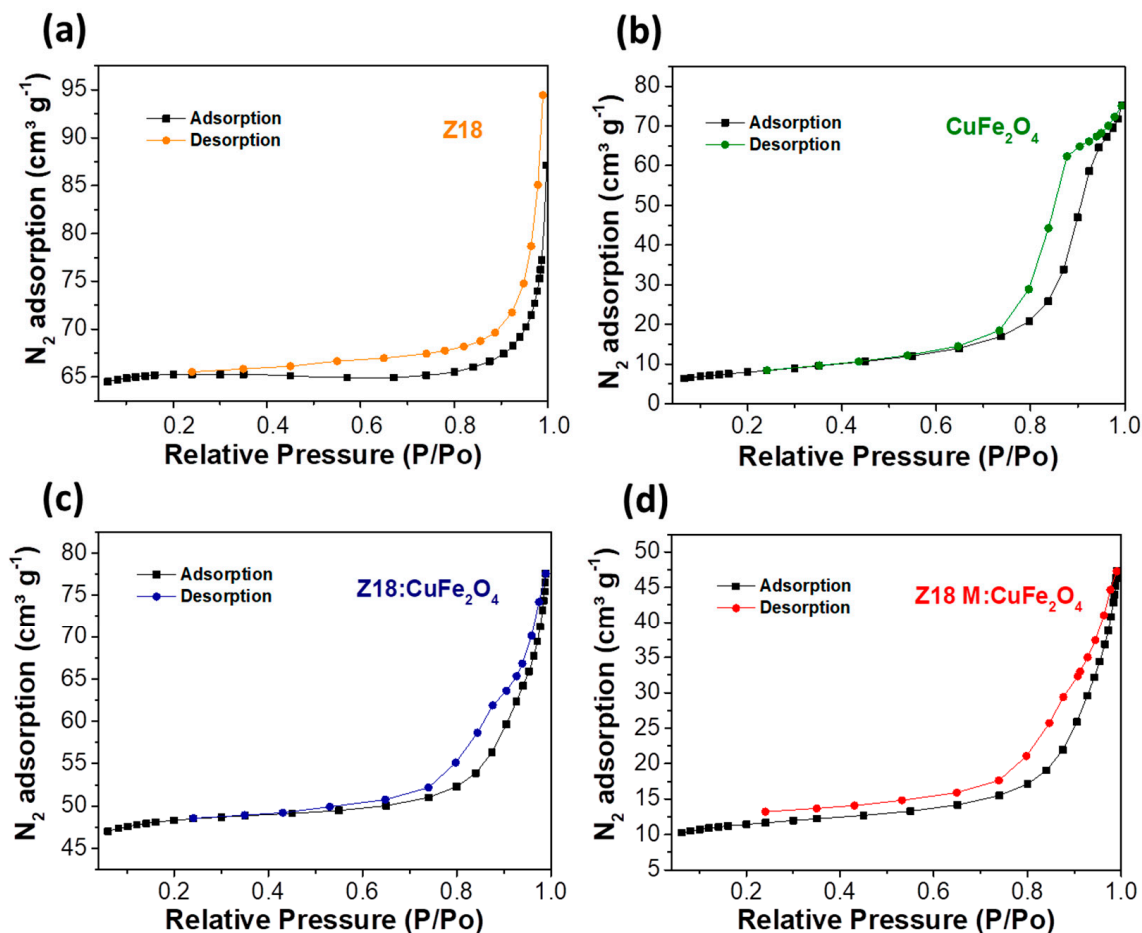


**Figure 9.** TEM analysis: (a) Z18:CuFe<sub>2</sub>O<sub>4</sub> images; electron diffraction pattern (reciprocal lattice) for (b) Z18 and (c) Z18:CuFe<sub>2</sub>O<sub>4</sub>.

The stability of the aqueous dispersions in the investigated samples was evaluated through zeta potential ( $\zeta$ ) measurements. The Z18 dispersion pH was 7.8, and the zeolite had a negative surface charge ( $\zeta = -38.9$  mV) [58,59]. Possibly, Z18 was actually above its isoelectric point; hence, it is expected to be negatively charged because of surface OH deprotonation. Therefore, zeolite stability in aqueous media is  $\zeta$  greater than  $\pm 30$  mV [60]. Regarding CuFe<sub>2</sub>O<sub>4</sub>, a zeta potential of  $-22$  mV was measured, placing the magnetic material below the ( $\zeta$ ) stability threshold in aqueous solutions. Concerning the composite materials, the measured zeta potentials were  $-50.9$  mV and  $19.7$  mV for Z18:CuFe<sub>2</sub>O<sub>4</sub> and Z18 M:CuFe<sub>2</sub>O<sub>4</sub>, respectively. It can be inferred that, with Z18:CuFe<sub>2</sub>O<sub>4</sub> dispersion pH still being slightly basic (7.8), both zeolite OH surface groups are deprotonated. Such findings may justify Z18:CuFe<sub>2</sub>O<sub>4</sub>  $\zeta$  negative values. On the contrary, Z18 M:CuFe<sub>2</sub>O<sub>4</sub> zeta potential is being affected by surface modification. The presence of the N-H group, which had a positive charge on the zeolite surface from APTES modification and a pH reduction to 6.7 that led to OH groups protonation, may have affected the zeta potential and justified the Z18 M:CuFe<sub>2</sub>O<sub>4</sub> positive charge [61]. Furthermore, the slightly acidic pH may contribute to the zeolite surface protonation and, therefore, to the positive zeta potential.

N<sub>2</sub> adsorption/desorption curves and pore size measurements (Figure 10 and Table 1) reflect the different morphology, composition, and processing of the studied materials, in accordance with the IUPAC Technical Report [62]. Samples containing Z18 present a Type IV isotherm, typical of mesoporous materials. On the other hand, the pure copper ferrite isotherm resembles a Type V curve, still associated with a mesoporous material but demonstrates a weak substrate-adsorbate interaction. Capillary condensation (manifesting as a hysteresis loop accounting for most of the surface coverage in Type-V materials) occurs at a higher relative pressure (i.e., hysteresis loop shifting) in CuFe<sub>2</sub>O<sub>4</sub> than in the Z18 and the other zeolite-containing composites. Furthermore, the pure zeolite manifests a clear adsorption “knee point” corresponding to forming a monolayer of gas molecules. At the same time, by contrast, such a feature tends to swindle as CuFe<sub>2</sub>O<sub>4</sub> is introduced in the

zeolitic material. Moreover, the pristine copper ferrite presents an H2 hysteresis, usually signifying that the pore size and shape distribution are not well defined.



**Figure 10.**  $N_2$  adsorption/desorption isotherms of the samples: (a) Z18, (b)  $CuFe_2O_4$ , (c,d) Z18: $CuFe_2O_4$ , and Z18 M: $CuFe_2O_4$ .

**Table 1.** Parameters of BET analysis of zeolite, ferrite, and composites.

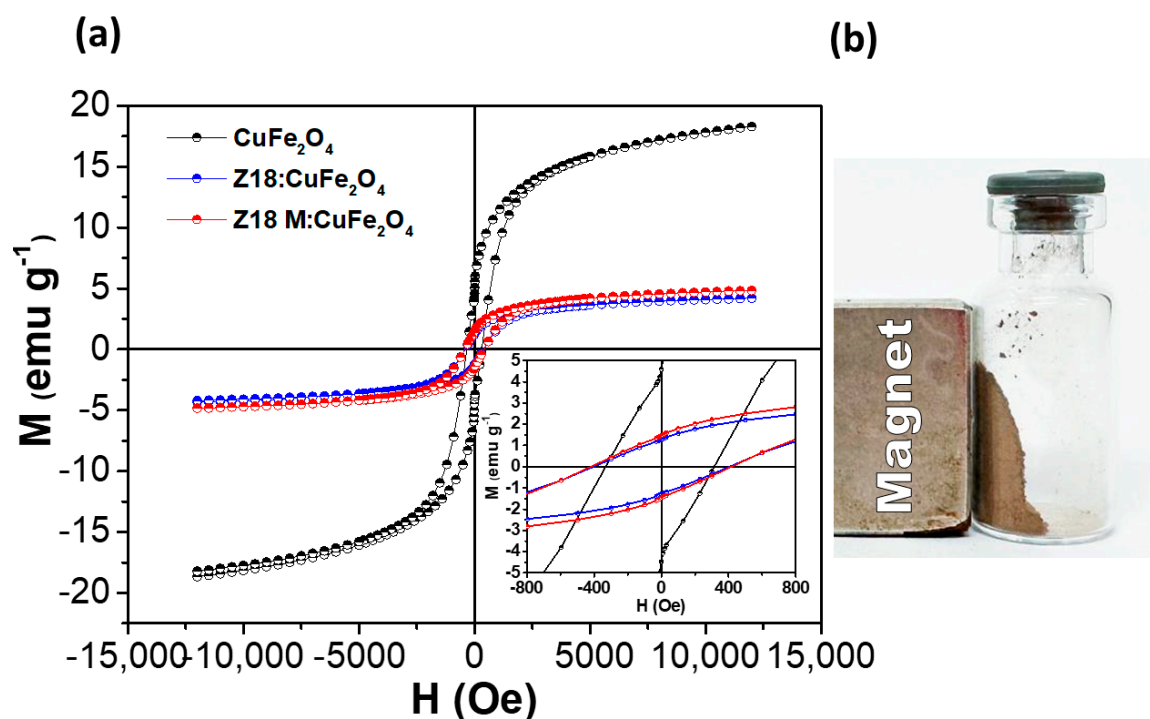
Samples	$SSA_{BET}$ ( $m^2 g^{-1}$ )	$A_{micropore}$ ( $m^2 g^{-1}$ )	$D_{pore}$ (nm)
Z18	218	208	27.5
$CuFe_2O_4$	28	4	12.2
Z18: $CuFe_2O_4$	162	144	16.0
Z18 M: $CuFe_2O_4$	39	22	15.7

Conversely, an H3 hysteresis revealing slit-shaped pores was observed for Z18 and its ilk. The variation in the specific surface area (SSA) and micropore area values among the different materials was quite relevant. For instance,  $CuFe_2O_4$  displayed the lowest SSA ( $28 m^2 g^{-1}$ ) with a negligible fraction ascribable to micropores. Such a picture is in accordance with the SEM analysis showing particle agglomeration. Furthermore, low specific area values of magnetic materials (compared to established absorbers like zeolites, silica, and activated carbon) have already been reported [38,63]. Z18 possessed the highest SSA,  $218 m^2 g^{-1}$ , with a considerable contribution from micropores. Not surprisingly, the Z18: $CuFe_2O_4$  SSA was reduced by the lower contribution to the total area stemming from the copper ferrite. Similarly, the SSA dropped to  $39 m^2 g^{-1}$  after Z18 modification (Z18 M). Silane groups probably hampered nitrogen access to the inner pores of the material (i.e., partial pore blocking) [64,65]. As for the average diameter of the pore size, Z18 was



discovered to be on the mesoporous lower limit (2–50 nm), whereas  $\text{CuFe}_2\text{O}_4$  possessed the smaller pores (12.2 nm). Reasonably, ferrite pores result from interparticle porosity rather than defined material mesopores. Plausibly, the two composite materials' average pore sizes lay in between Z18 and  $\text{CuFe}_2\text{O}_4$ , giving two intermediate values close to 16 nm.

The magnetic properties of the  $\text{CuFe}_2\text{O}_4$  particles and the magnetic zeolite composites are shown in Figure 11a, showing the field-dependent magnetization loops measured at 26.85 °C. Bare ferrite particles exhibit a saturation magnetization ( $M_s$ ) of  $15.4 \text{ emu g}^{-1}$ , which is significantly higher than the values reported in the literature for copper ferrite particles synthesized via coprecipitation with heat treatment at 500 °C, a method similar to that used in the present work [66]. It is worth mentioning that the actual  $M_s$  might exceed the measured value due to sample geometric effects. However, such effects cannot be accurately accounted for due to the irregular shape of the sample. In fact, specific measurement protocols, which cannot be performed with the magnetometer used in this study, should be implemented [67]. Pure zeolites exhibit diamagnetic properties prior to the addition of magnetic nanoparticles, in agreement with data reported in the literature [50]. Upon the  $\text{CuFe}_2\text{O}_4$  immobilization, the magnetic nanocomposite with zeolites exhibits ferrimagnetic behavior [68], with an effective saturation magnetization of 3.5 and  $4.1 \text{ emu g}^{-1}$  for samples Z18: $\text{CuFe}_2\text{O}_4$  and Z18 M: $\text{CuFe}_2\text{O}_4$ , respectively.

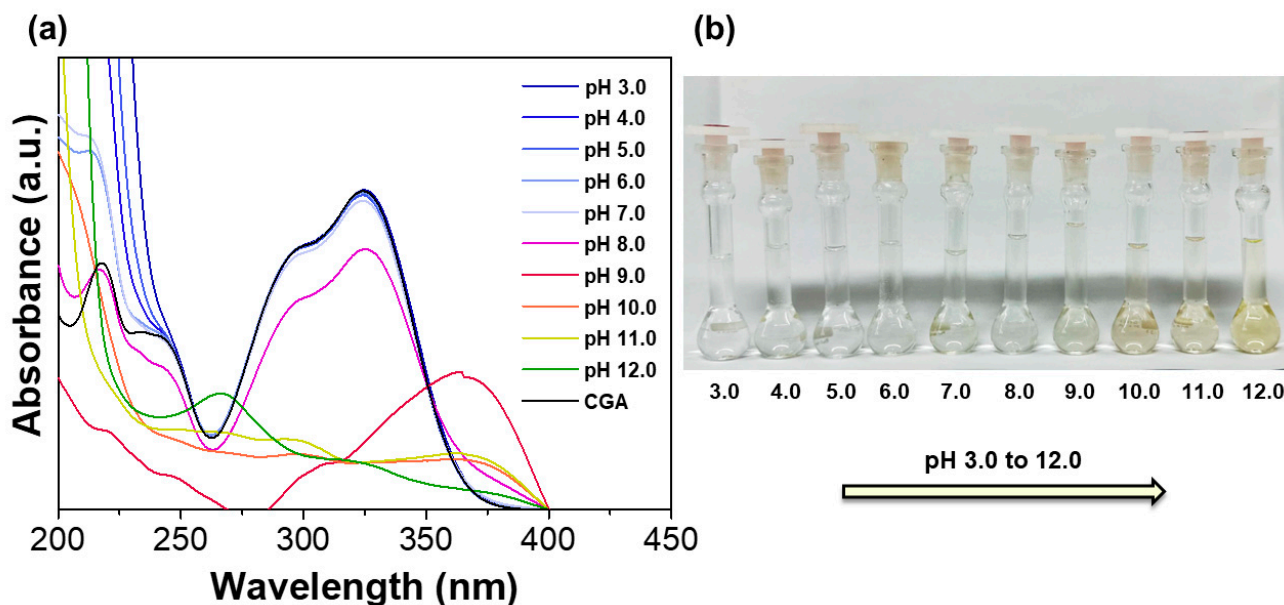


**Figure 11.** Magnetic hysteresis curves for (a) pristine ferrite and nanocomposite materials; (b) Z18M: $\text{CuFe}_2\text{O}_4$  behavior in the presence of a permanent magnet.

As the weight percentage of magnetic particles in the zeolite composites is approximately 25%, the saturation magnetization normalized to the wt% of ferrite particles in the composite ( $14$  and  $16.4 \text{ emu g}^{-1}$  for samples Z18: $\text{CuFe}_2\text{O}_4$  and Z18 M: $\text{CuFe}_2\text{O}_4$ , respectively) is comparable to the values of pristine powders. This suggests that the magnetic particles are unaffected by the incorporation process, and the observed reduction in magnetization can be ascribed solely to the presence of the diamagnetic zeolite matrix. The saturation magnetization of the composites aligns closely with those reported in the literature for other magnetic zeolites [34,69,70]. It is sufficiently high to facilitate their manipulation by applying an external magnetic field (Figure 11b). Thus, incorporating

magnetic particles imparts magnetic functionality to the zeolite derived from rice husk waste, enabling their removal by magnetic separation.

The two magnetic nanocomposites, with and without surface modification, were tested for CGA adsorption in aqueous media to assess the influence of surface functionalization with hydrophobic groups on the removal efficiency. As previously mentioned, the CGA UV absorbance dependence on pH was preliminarily investigated. Figure 12 shows the UV-Vis spectra of CGA at a concentration of  $20 \text{ mg L}^{-1}$  and different pHs. The analysis showed a change in the CGA spectrum for pH values above 7.0, showing greater instability in alkaline solutions.

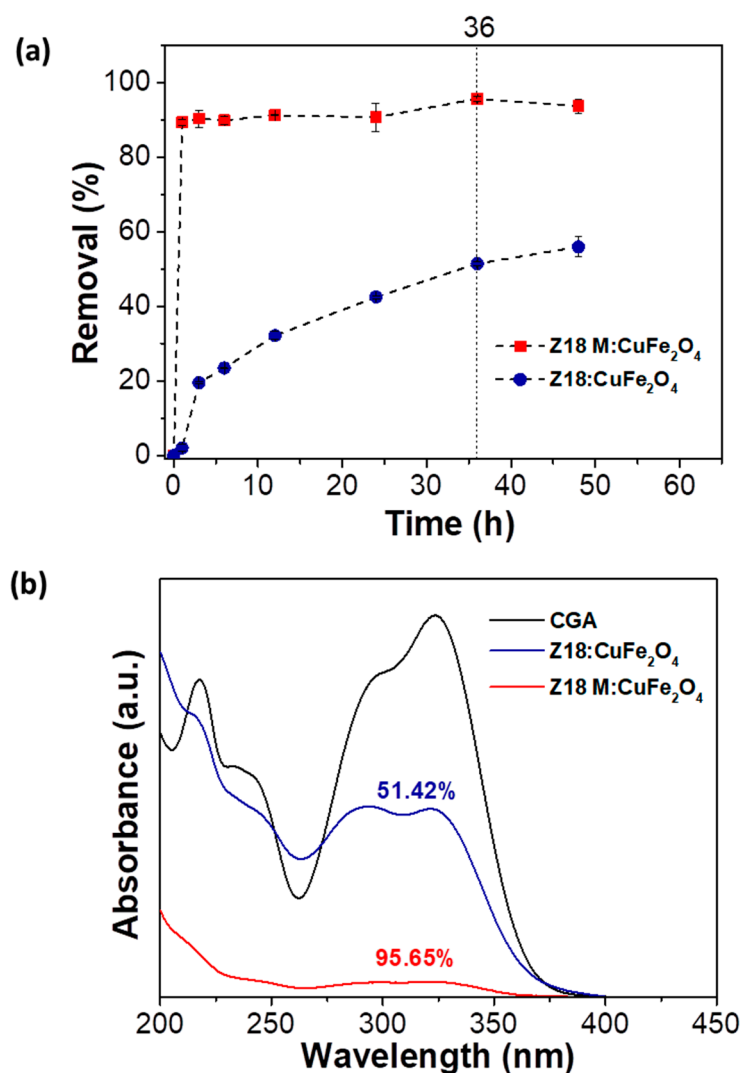


**Figure 12.** CGA chemical behavior as pH varies in the range of 3.0–12.0: (a) UV-Vis spectra and (b) aqueous solutions.

The change in the spectrum profile (Figure 12a) may be correlated to the CGA protonation–deprotonation equilibrium in aqueous media and the formation of its possible isomers [7]. In addition, a color change (i.e., yellowish tinted solution) was uncovered for pH = 9.0, 10.0, 11.0, and 12.0 solutions. In addition, the higher the pH, the more intense the color change, as illustrated in Figure 12b. Previous works have reported the CGA UV-Vis absorption spectra shift (and mutation in chromatographic properties) when the pH drifts towards alkaline conditions [41,71]. Hence, to ensure the reliability of the results, after adsorption, the aliquots were adjusted to pH = 5 with a phosphate buffer solution (sample: buffer ratio 3:1) for the UV-Vis spectrum to revert to the original CGA profile. Then, the spectrum was analyzed in the 200–425 nm region. The phosphate buffer enabled the acquisition of the characteristic CGA spectrum and, consequently, the effective calculation of the adsorption rate of the nanocomposites.

The CGA removal rate was evaluated based on the contact time with the adsorbents at room temperature. As illustrated in Figure 13a, the modified composite (Z18 M:CuFe<sub>2</sub>O<sub>4</sub>) showed better polyphenol adsorption performances, achieving a removal rate of 89.35% in an hour. At the same time, the percentage of CGA removed by Z18:CuFe<sub>2</sub>O<sub>4</sub> was almost immaterial, amounting to a mere 2.03%. Over time, both composites tended towards the saturation of the adsorption sites; however, after 36 h, RR (%) was 95.65% for Z18 M:CuFe<sub>2</sub>O<sub>4</sub>, whereas Z18:CuFe<sub>2</sub>O<sub>4</sub> could not pass 51.42% (Figure 13b). Still, the unmodified adsorbent did not saturate even after 50 h. Therefore, the apparent SSA is not the only parameter in CGA adsorption. Despite a smaller SSA, Z18 M:CuFe<sub>2</sub>O<sub>4</sub> could rapidly remove CGA from the solution. Indeed, TMCS and APTES methyl and propyl groups made the zeolite surface partly hydrophobic, favoring the interaction with CGA. Furthermore,

amine and chloride groups may promote anchorage on the organic part's zeolite surface, leading to a stable functionalization of FAU and GIS. In addition,  $\text{NH}_2$  groups may establish H-bonds with CGA phenol OH groups. Thus, zeolite large surface area, in conjunction with hydrophobically functionalized absorption sites, may account for Z18 M:CuFe<sub>2</sub>O<sub>4</sub> being able to quickly and almost completely remove CGA. Finally, the Z18 M:CuFe<sub>2</sub>O<sub>4</sub> positive zeta potential, and by extension, positive surface charges, are conducive to electrostatic interaction with the CGA carboxylic group, provided it is ionized. Contrary to this, the dissociation of phenolic groups ought to be safely ruled out.



**Figure 13.** CGA adsorption study: (a) contact time effect and (b) UV-Vis spectra after 36 h adsorption.

The adsorption on Z18:CuFe<sub>2</sub>O<sub>4</sub> can benefit only from hydrogen bonds between Z18 surface hydroxyl groups and CGA phenolic and carboxylic OHs. Indeed, the negative  $\zeta$  is supposed to hamper surface attraction with CGA carboxylate. The unmodified zeolite composite also manifests slower adsorption kinetics, requiring longer times to reach equilibrium. In this sense, modification is instrumental in facilitating CGA adsorption since it promotes the formation of active sites on the zeolite surface. On the other hand, the pore size of the two composite materials (i.e., related to steric hindrance) should not matter when it comes to CGA adsorption, with the average pore diameter being very close and allowing for CGA molecule dimensions.

The kinetic model analysis (Figure 14) indicated that Z18 M:CuFe<sub>2</sub>O<sub>4</sub> followed a pseudo-second-order kinetic profile ( $R^2 = 0.9995$ ), while Z18:CuFe<sub>2</sub>O<sub>4</sub> matched a pseudo-

first-order model ( $R^2 = 0.9684$ ). This change in the kinetic order of the composites can be attributed to the modification of the adsorbent surface. Modification with APTES and TMCS increases the affinity for the CGA molecule, introducing more specific adsorption sites and more complex interactions with the adsorbate, which justifies second-order kinetics. The experimental adsorption capacities ( $q_e$ ) were extremely close to those calculated (Table 2). In particular, the amount of Z18 M:CuFe<sub>2</sub>O<sub>4</sub> measured and extrapolated  $q_e$  was 9.56 and 9.43 mg g<sup>-1</sup>, respectively. The adsorption capacity was more prominent for the modified sample than the composite without modification ( $q_e = 5.14$  mg g<sup>-1</sup>). The pseudo-second-order rate constant ( $k_2$ ) of the composite modified with APTES and TMCS presented an impressively high value of 0.5140 g mg<sup>-1</sup> min<sup>-1</sup>, which is 50 times higher than that the one reported in the literature for CGA adsorption on APTES-functionalized SiO<sub>2</sub> [72]. Because of the high kinetic parameters, implying a solid adsorbent–adsorbate affinity (e.g., hydrophobic interaction, electrostatic attraction, and hydrogen bond), it can be hypothesized that CGA takes place by chemisorption [73,74].

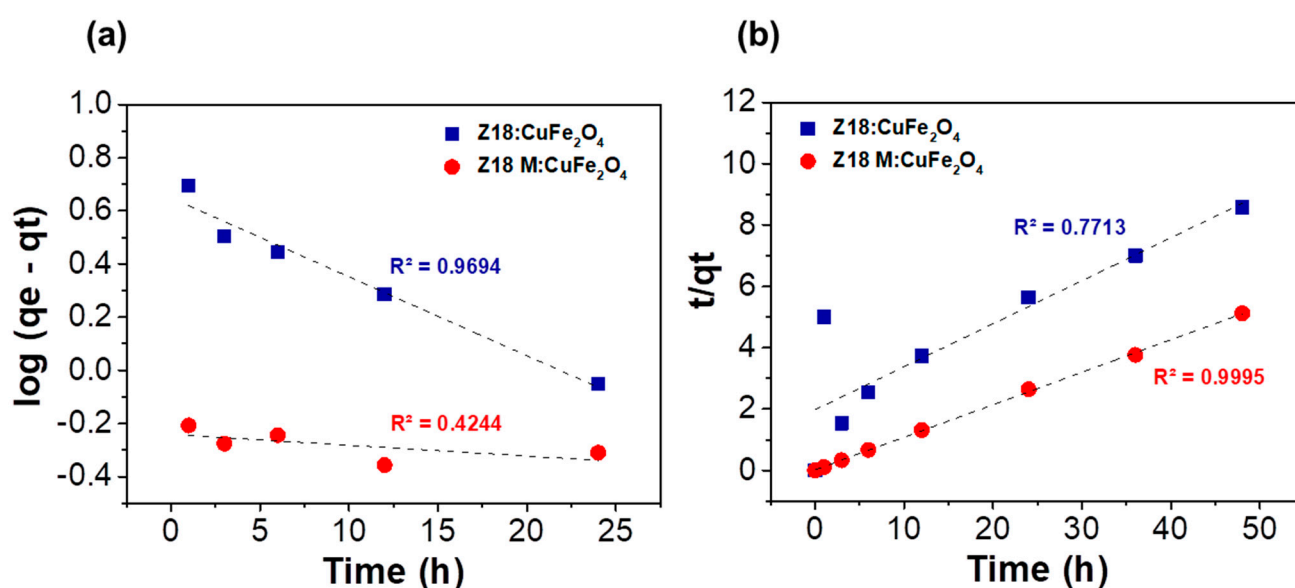
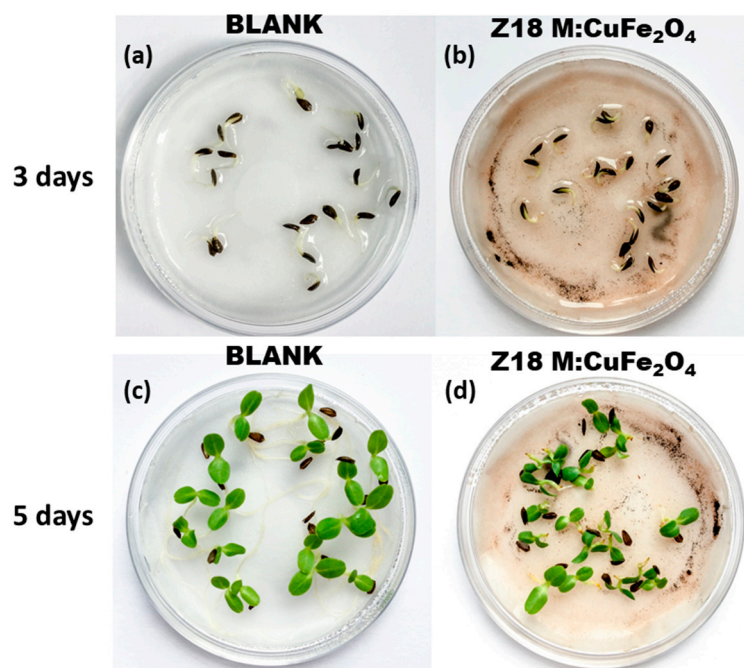


Figure 14. CGA adsorption kinetic models: (a) pseudo-first-order and (b) pseudo-second-order.

Table 2. Kinetic parameters of CGA adsorption with the magnetic nanocomposites Z18:CuFe<sub>2</sub>O<sub>4</sub> and Z18 M:CuFe<sub>2</sub>O<sub>4</sub>.

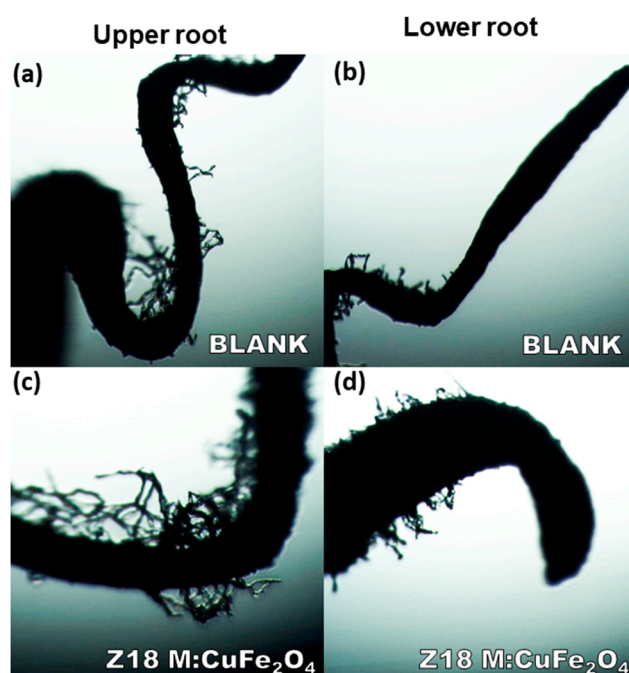
Nanocomposites	Experimental		Pseudo-First-Order		Pseudo-Second-Order		
	$q_e$ (mg g <sup>-1</sup> )	$q_e$ (mg g <sup>-1</sup> )	$k_1$ (min <sup>-1</sup> )	$R^2$	$q_e$ (mg g <sup>-1</sup> )	$k_2$ (g mg <sup>-1</sup> min <sup>-1</sup> )	$R^2$
Z18:CuFe <sub>2</sub> O <sub>4</sub>	5.14	4.46	0.0684	0.9694	7.13	0.0099	0.7713
Z18 M:CuFe <sub>2</sub> O <sub>4</sub>	9.56	9.43	0.0094	0.4244	9.43	0.5140	0.9995

Despite excellent adsorbing performance, before using Z18 M:CuFe<sub>2</sub>O<sub>4</sub> for water remediation, the possible harmful environmental effects connected to nanoparticles and organosilane functionalities should be considered. Therefore, a Z18 M:CuFe<sub>2</sub>O<sub>4</sub> germination test was evaluated by lettuce seeds (*Lactuca sativa*). Specifically, root development was appraised after exposure to Z18 M:CuFe<sub>2</sub>O<sub>4</sub>. Figure 15 compares the germination in water (blank) and in contact with a Z18 M:CuFe<sub>2</sub>O<sub>4</sub> suspension. It can be observed that seeds germinated in three days and shoots appeared in five days, showing no inhibition of germination caused by the nanocomposite.



**Figure 15.** Germination of lettuce (*Lactuca sativa*) seeds in water (a) Blank in 3 days and (b) Z18 M:CuFe<sub>2</sub>O<sub>4</sub> in 3 days; (c) blank in 5 days and (d) Z18 M: CuFe<sub>2</sub>O<sub>4</sub> in 5 days.

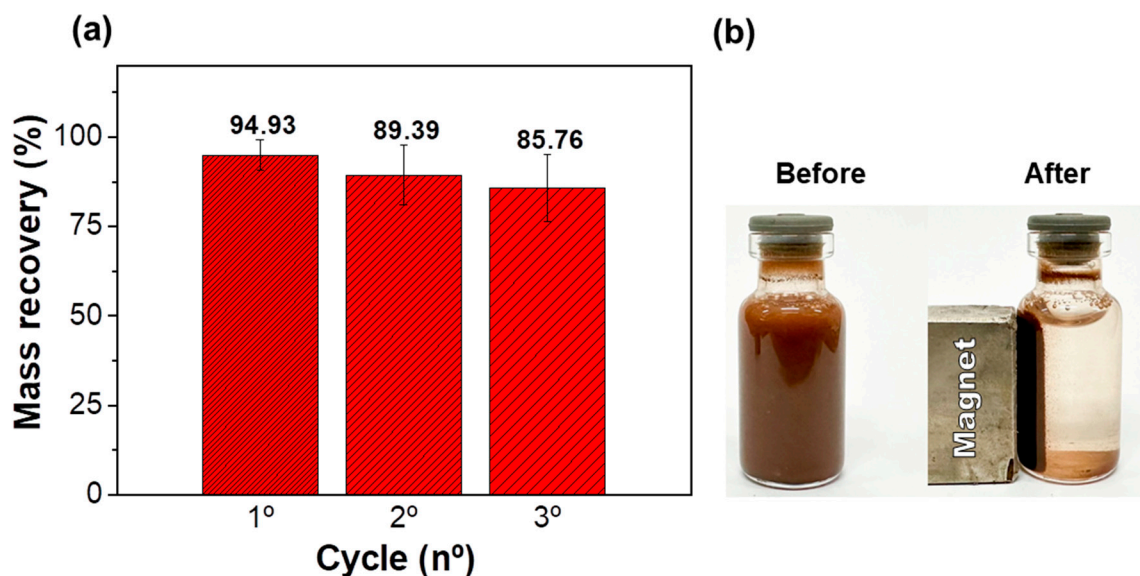
It can also be observed (Figure 16a–d) that after 5 days of germination, the rootlets are already visible and evident. This appearance of rootlets signifies healthy development in the presence of the particulate nanomaterial. This fact demonstrates no detrimental effect during seed germination brought about by the organosilanes or the nanostructured zeolite:CuFe<sub>2</sub>O<sub>4</sub> pair. Optical microscopic images show the difference in the thickness of the upper and lower roots, which is in line with the expected pattern for an ideal stage of plant growth.



**Figure 16.** Optical microscopy images of lettuce (*Lactuca sativa*) roots after a 5-day germination period from seeds exposed to (a,b) water (blank) and the sample (c,d) Z18 M:CuFe<sub>2</sub>O<sub>4</sub>.



In order to separate the adsorbent from the aqueous medium after the CGA adsorption process, a mass recovery test was carried out on Z18 M:CuFe<sub>2</sub>O<sub>4</sub> (Figure 17). The analysis revealed a remarkable mass recovery percentage of the nanocomposite, given that the major component (zeolite:copper ferrite ratio equal to 3 to 1) is non-magnetic. The Z18 M:CuFe<sub>2</sub>O<sub>4</sub> sample showed a mass recovery of 94.93%, 89.39%, and 85.76% in the 1<sup>o</sup>, 2<sup>o</sup>, and 3<sup>o</sup> immersion cycles, respectively. Although a mass loss of around 5% per cycle was observed, this rate is considered acceptable for the studied materials, given the magnetic nature of the recovery process. Despite this loss, the material retains sufficient mass after cycling, rendering it amenable to practical applications, especially when compared to other composites in the literature [17].



**Figure 17.** Nanocomposite Z18M:CuFe<sub>2</sub>O<sub>4</sub>. (a) Mass recovery % via magnetic separation with neodymium magnet; (b) Z18 M:CuFe<sub>2</sub>O<sub>4</sub> suspension before and after magnetic field application.

In addition to the relatively high mass recovery efficiency of the magnetic nanocomposites, the choice of copper ferrite as the magnetic component stands out for several reasons. Its low toxicity and its potential as a micronutrient for soil are important characteristics since any eventual loss of adsorbent in the environment could benefit agriculture [75]. Copper ferrites also have excellent catalytic activity and adsorption capacity, contributing to the efficient removal of pollutants [76,77]. Finally, this study serves as a “proof of concept” for using bornite tailings (Cu<sub>5</sub>FeS<sub>4</sub>) from the northeast of Brazil, with a goal to advance the sustainable production of magnetic ferrites.

#### 4. Conclusions

A magnetic zeolite:copper ferrite composite was prepared using agricultural waste. In particular, high-purity silica obtained from rice husks by a simple leaching/annealing procedure proved to be a viable choice for the sustainable synthesis of zeolites meant for environmental remediation. In addition, an enhanced, modified zeolite magnetic composite (Z18 M:CuFe<sub>2</sub>O<sub>4</sub>) with a magnetic saturation (*M<sub>s</sub>*) value of 4.1 emu g<sup>-1</sup> was devised and fabricated by using organosilane (TMCS:APTES mixture) surface functionalization. Z18 M:CuFe<sub>2</sub>O<sub>4</sub> was highly effective in removing CGA from water media. The modified nanocomposite presented a CGA overall adsorption rate of 95.65% and fast pseudo-second-order kinetics, with a rate constant of 0.5140 g mg<sup>-1</sup> min<sup>-1</sup>. These results probably stem from the superimposition of the hydrophobic interaction between CGA and the adsorbent, hydrogen bond, and electrostatic attraction originating from the Z18 M:CuFe<sub>2</sub>O<sub>4</sub> positive zeta potential. Furthermore, the material manifested a mass recovery of over 85% after three cycles of water immersion, which was achieved by applying an external magnetic

field. These characteristics contribute to the implementation of a sustainable wastewater treatment system with the potential for large-scale production, especially regarding polyphenols in the food industry. Although the material was tested in a controlled laboratory environment, the promising results suggest its potential applicability in real-world industrial wastewater treatment, warranting further investigation under actual conditions. Consequently, the present composite material may represent a valuable contribution to the circular economy, being a low-cost/low-end adsorbent (suitable for re-utilization) attained from a byproduct whose output measures up to hundreds of millions of tons per year worldwide.

**Author Contributions:** Conceptualization, T.R.N., S.Q., S.A.D.F. and E.C.P.; Methodology, T.R.N., L.F.L.S., M.L.L.S.e.S. and V.V.V.V.; Software, T.R.N. and M.L.L.S.e.S.; Validation, T.R.N., L.F.L.S., S.A.D.F. and E.C.P.; Formal Analysis, T.R.N., C.D.C., F.M., M.R., G.V., M.A. and S.Q.; Investigation, T.R.N., L.F.L.S., M.L.L.S.e.S., S.A.D.F. and E.C.P.; Resources, E.C.P.; Data Curation, T.R.N. and E.C.P.; Writing—Original Draft Preparation, T.R.N.; Writing—Review and Editing, T.R.N., L.F.L.S., S.Q., S.A.D.F. and E.C.P.; Visualization, T.R.N. and E.C.P.; Supervision, E.C.P.; Project Administration, E.C.P.; Funding Acquisition, E.C.P. All authors have read and agreed to the published version of the manuscript.

**Funding:** This research was funded by the Conselho Nacional de Desenvolvimento Científico e Tecnológico (CNPq), process number 165522/2021-6, SisNano, FINEP, AgroNano Network, and Embrapa (Grant number 11.14.03.001.01.00). The APC was funded by Embrapa.

**Institutional Review Board Statement:** Not applicable.

**Informed Consent Statement:** Not applicable.

**Data Availability Statement:** The original data presented in this study are available on reasonable request from the corresponding author. The data are not publicly available due to privacy.

**Acknowledgments:** We would like to thank Adriana Coatrini Thomazi and Viviane Faria Soares (Embrapa, Brazil) for their technical support and valuable discussions during the analyses, Davide Peddis (University of Genova, Italy) for his insights and discussion on magnetic properties, and Fulvio Federici and Enrico Patrizi (CNR) for their technical assistance. Furthermore, we thank Alessandro Latini and Marco Agostini (Sapienza University of Rome) for the TEM analysis. TEM investigation was carried out with the support of the «Advanced Tomography and Microscopy» (ATOM) project granted by Lazio Region (protocol number #173-2017-17395 L:R: 13/2008).

**Conflicts of Interest:** The authors declare no conflicts of interest.

## References

1. Mader, A.E.; Holtman, G.A.; Welz, P.J. Treatment Wetlands and Phyto-Technologies for Remediation of Winery Effluent: Challenges and Opportunities. *Sci. Total Environ.* **2022**, *807*, 150544. [[CrossRef](#)] [[PubMed](#)]
2. Cuffaro, D.; Bertolini, A.; Bertini, S.; Ricci, C.; Cascone, M.G.; Danti, S.; Saba, A.; Macchia, M.; Digiaco, M. Olive Mill Wastewater as Source of Polyphenols with Nutraceutical Properties. *Nutrients* **2023**, *15*, 3746. [[CrossRef](#)] [[PubMed](#)]
3. Hamimed, S.; Kthiri, A. Potential Valorization of Polyphenols from Olive Mill Wastewater on Sheep Rumen Function. *Int. J. Environ. Sci. Technol.* **2022**. [[CrossRef](#)]
4. Athanasiadis, V.; Voulgaris, A.; Katsoulis, K.; Lalas, S.I.; Roussis, I.G.; Gortzi, O. Development of Enriched Oil with Polyphenols Extracted from Olive Mill Wastewater. *Foods* **2023**, *12*, 497. [[CrossRef](#)]
5. Sas, O.G.; Castro, M.; Domínguez, Á.; González, B. Removing Phenolic Pollutants Using Deep Eutectic Solvents. *Sep. Purif. Technol.* **2019**, *227*, 115703. [[CrossRef](#)]
6. Ramos, L.F.; Pluschke, J.; Bernardes, A.M.; Geißen, S.-U. Polyphenols in Food Processing Wastewaters: A Review on Their Identification and Recovery. *Clean. Circ. Bioeconomy* **2023**, *5*, 100048. [[CrossRef](#)]
7. Dawidowicz, A.L.; Typek, R. The Influence of PH on the Thermal Stability of 5-O-Caffeoylquinic Acids in Aqueous Solutions. *Eur. Food Res. Technol.* **2011**, *233*, 223–232. [[CrossRef](#)]
8. Hernández-Padilla, E.S.; Zárate-Guzmán, A.I.; González-Ortega, O.; Padilla-Ortega, E.; Gómez-Durán, A.; Delgado-Sánchez, P.; Aguilar-Aguilar, A.; Cortés, F.B.; Ocampo-Pérez, R. Elucidation of Adsorption Mechanisms and Mass Transfer Controlling Resistances during Single and Binary Adsorption of Caffeic and Chlorogenic Acids. *Environ. Sci. Pollut. Res.* **2022**, *29*, 26297–26311. [[CrossRef](#)]
9. Wang, L.; Pan, X.; Jiang, L.; Chu, Y.; Gao, S.; Jiang, X.; Zhang, Y.; Chen, Y.; Luo, S.; Peng, C. The Biological Activity Mechanism of Chlorogenic Acid and Its Applications in Food Industry: A Review. *Front. Nutr.* **2022**, *9*, 943911. [[CrossRef](#)]

10. Zhang, J.; Zhang, S.; Wu, J.; Li, N.; Wang, J. Separation and Purification of Chlorogenic Acid from *Lonicera Japonica* Thunb. Leaves Exact with Macroporous Resins. *J. Med. Plants Res.* **2013**, *7*, 1784–1792. [[CrossRef](#)]
11. Shen, Z.; Ji, X.; Yao, S.; Zhang, H.; Xiong, L.; Li, H.; Chen, X.; Chen, X. Study on the Adsorption Behavior of Chlorogenic Acid from *Eucommia Ulmoides* Oliver Leaf Extract by a Self-Synthesized Resin. *Ind. Crops Prod.* **2023**, *197*, 116585. [[CrossRef](#)]
12. Rodriguez-Lopez, A.D.; Reig, M.; Mayor, L.; Ortiz-Climent, M.; Garcia-Castello, E.M. Characterization of Ionic Exchange and Macroporous Resins for Their Application on the Separation and Recovery of Chlorogenic Acid from the Wastewater of Artichoke Blanching. *Sustainability* **2021**, *13*, 8928. [[CrossRef](#)]
13. Mora-Villalobos, J.A.; Aguilar, F.; Carballo-Arce, A.F.; Vega-Baudrit, J.R.; Trimino-Vazquez, H.; Villegas-Peñaranda, L.R.; Stöbener, A.; Eixenberger, D.; Bubenheim, P.; Sandoval-Barrantes, M.; et al. Tropical Agroindustrial Biowaste Revalorization through Integrative Biorefineries—Review Part I: Coffee and Palm Oil by-Products. *Biomass Convers. Biorefinery* **2023**, *13*, 1469–1487. [[CrossRef](#)]
14. Tapia-Quirós, P.; Montenegro-Landívar, M.F.; Reig, M.; Vecino, X.; Cortina, J.L.; Saurina, J.; Granados, M. Recovery of Polyphenols from Agri-Food By-Products: The Olive Oil and Winery Industries Cases. *Foods* **2022**, *11*, 362. [[CrossRef](#)] [[PubMed](#)]
15. Ijanu, E.M.; Kamaruddin, M.A.; Norashiddin, F.A. Coffee Processing Wastewater Treatment: A Critical Review on Current Treatment Technologies with a Proposed Alternative. *Appl. Water Sci.* **2020**, *10*, 11. [[CrossRef](#)]
16. Paris, E.C.; Malafatti, J.O.D.; Musetti, H.C.; Manzoli, A.; Zenatti, A.; Escote, M.T. Faujasite Zeolite Decorated with Cobalt Ferrite Nanoparticles for Improving Removal and Reuse in Pb<sup>2+</sup> Ions Adsorption. *Chin. J. Chem. Eng.* **2020**, *28*, 1884–1890. [[CrossRef](#)]
17. Meirelles, M.R.; Malafatti, J.O.D.; Escote, M.T.; Pinto, A.H.; Paris, E.C. Magnetic Adsorbent Based on Faujasite Zeolite Decorated with Magnesium Ferrite Nanoparticles for Metal Ion Removal. *Magnetochemistry* **2023**, *9*, 136. [[CrossRef](#)]
18. Malamis, S.; Katsou, E. A Review on Zinc and Nickel Adsorption on Natural and Modified Zeolite, Bentonite and Vermiculite: Examination of Process Parameters, Kinetics and Isotherms. *J. Hazard. Mater.* **2013**, *252–253*, 428–461. [[CrossRef](#)]
19. Lee, J.B.; Ahmed, I.; Lee, G.; Kim, T.W.; Kim, C.U.; Jhung, S.H. Synthesis of SSZ-13 Zeolites Using Calcined Rice Husk as Silica Source for Propylene Production from Ethylene and Carbon Dioxide Adsorption. *J. Ind. Eng. Chem.* **2023**, *128*, 443–449. [[CrossRef](#)]
20. Cheng, Y.; Xu, L.; Jiang, Z.; Liu, C.; Zhang, Q.; Zou, Y.; Chen, Y.; Li, J.; Liu, X. Feasible Low-Cost Conversion of Red Mud into Magnetically Separated and Recycled Hybrid SrFe<sub>12</sub>O<sub>19</sub>@NaP1 Zeolite as a Novel Wastewater Adsorbent. *Chem. Eng. J.* **2021**, *417*, 128090. [[CrossRef](#)]
21. Ponce, J.; da Silva Andrade, J.G.; dos Santos, L.N.; Bulla, M.K.; Barros, B.C.B.; Favaro, S.L.; Hioka, N.; Caetano, W.; Batistela, V.R. Alkali Pretreated Sugarcane Bagasse, Rice Husk and Corn Husk Wastes as Lignocellulosic Biosorbents for Dyes. *Carbohydr. Polym. Technol. Appl.* **2021**, *2*, 100061. [[CrossRef](#)]
22. Durand, K.; Daassi, R.; Rodrigue, D.; Stevanovic, T. Study of Biopolymers and Silica Recovery from Pre-Hydrolyzed Rice Husks. *Biomass Convers. Biorefinery* **2024**. [[CrossRef](#)]
23. Joshi, U.; Roy, R.; Bhosale, P.; Nikam, S.; Kamble, T.; Satsangi, P.G. Sustainable Economic Production of Silica Nanoparticles from Rice Husks for Adsorptive Removal of Anionic and Cationic Dyes. *Bioresour. Technol. Rep.* **2023**, *24*, 101685. [[CrossRef](#)]
24. Chanda, R.; Islam, M.S.; Biswas, B.K. N and P Removal from Wastewater Using Rice Husk Ash-Derived Silica-Based Fe-ZSM-5 Zeolite. *Clean. Eng. Technol.* **2023**, *16*, 100675. [[CrossRef](#)]
25. Hamidi, R.; Tai, L.; Paglia, L.; Scarsella, M.; Damizia, M.; De Filippis, P.; Musivand, S.; de Caprariis, B. Hydrotreating of Oak Wood Bio-Crude Using Heterogeneous Hydrogen Producer over Y Zeolite Catalyst Synthesized from Rice Husk. *Energy Convers. Manag.* **2022**, *255*, 115348. [[CrossRef](#)]
26. Sangsuradet, S.; Tobarammekul, P.; Worathanakul, P. Modified Hierarchical Zeolite X Derived from Riceberry Rice Husk for Propionic Acid Adsorption. *Mater. Chem. Phys.* **2022**, *282*, 125933. [[CrossRef](#)]
27. Qin, Z.; Yuan, P.; Yang, S.; Liu, D.; He, H.; Zhu, J. Silylation of Al<sup>13</sup>-Intercalated Montmorillonite with Trimethylchlorosilane and Their Adsorption for Orange II. *Appl. Clay Sci.* **2014**, *99*, 229–236. [[CrossRef](#)]
28. Bonaccorsi, L.; Bruzzaniti, P.; Calabrese, L.; Proverbio, E. Organosilanes Functionalization of Alumino-Silica Zeolites for Water Adsorption Applications. *Microporous Mesoporous Mater.* **2016**, *234*, 113–119. [[CrossRef](#)]
29. Kadja, G.T.M.; Dwihermiati, E.; Sagita, F.; Mukhoibibah, K.; Umam, K.; Ledyastuti, M.; Radiman, C.L. Mercapto Functionalized-Natural Zeolites/PVDF Mixed Matrix Membrane for Enhanced Removal of Methylene Blue. *Inorg. Chem. Commun.* **2023**, *157*, 111263. [[CrossRef](#)]
30. Mascarenhas, B.C.; Tavares, F.A.; Paris, E.C. Functionalized Faujasite Zeolite Immobilized on Poly(Lactic Acid) Composite Fibers to Remove Dyes from Aqueous Media. *J. Appl. Polym. Sci.* **2020**, *137*, 48561. [[CrossRef](#)]
31. Hashemi, M.S.H.; Eslami, F.; Karimzadeh, R. Organic Contaminants Removal from Industrial Wastewater by CTAB Treated Synthetic Zeolite Y. *J. Environ. Manag.* **2019**, *233*, 785–792. [[CrossRef](#)] [[PubMed](#)]
32. Rather, S.; Bamufleh, H.S.; Alhumade, H.; Taimoor, A.A.; Saeed, U.; Al-Zahrani, A.A.; Lemine, O.M. Morphological, Structural, Surface, Thermal, Chemical, and Magnetic Properties of Al-Doped Nanostructured Copper Ferrites. *Ceram. Int.* **2023**, *49*, 20261–20272. [[CrossRef](#)]
33. Tudorache, F. Investigations on Microstructure, Electrical and Magnetic Properties of Copper Spinel Ferrite with WO<sub>3</sub> Addition for Applications in the Humidity Sensors. *Superlattices Microstruct.* **2018**, *116*, 131–140. [[CrossRef](#)]
34. Wang, L.; Zhang, L.; Wang, H.; Li, J.; Zhang, E.; Wu, E.; Wang, H.; Wang, X. Synthesis of a Novel Magnetic CuFe<sub>2</sub>O<sub>4</sub>/Zeolite Composite Catalyst and Its Catalytic Oxidation Performance. *Mater. Lett.* **2023**, *350*, 134908. [[CrossRef](#)]

35. Tripathy, A.; Nine, M.J.; Silva, F.S. Biosensing Platform on Ferrite Magnetic Nanoparticles: Synthesis, Functionalization, Mechanism and Applications. *Adv. Colloid Interface Sci.* **2021**, *290*, 102380. [[CrossRef](#)]
36. Wang, J.; Deng, Q.; Li, M.; Jiang, K.; Zhang, J.; Hu, Z.; Chu, J. Copper Ferrites@reduced Graphene Oxide Anode Materials for Advanced Lithium Storage Applications. *Sci. Rep.* **2017**, *7*, 1–12. [[CrossRef](#)]
37. Ghosh, S.; Das, P.S.; Biswas, M.; Samajdar, S.; Mukhopadhyay, J. Z-Scheme Ferrite Nanoparticle/Graphite Carbon Nitride Nanosheet Heterojunctions for Photocatalytic Hydrogen Evolution. *Int. J. Hydrogen Energy* **2024**. [[CrossRef](#)]
38. Kharazi, P.; Rahimi, R.; Rabbani, M. Copper Ferrite-Polyaniline Nanocomposite: Structural, Thermal, Magnetic and Dye Adsorption Properties. *Solid State Sci.* **2019**, *93*, 95–100. [[CrossRef](#)]
39. Malafatti, J.O.D.; Tavares, F.A.; Neves, T.R.; Mascarenhas, B.C.; Quaranta, S.; Paris, E.C. Modified Silica Nanoparticles from Rice Husk Supported on Polylactic Acid as Adsorptive Membranes for Dye Removal. *Materials* **2023**, *16*, 2429. [[CrossRef](#)]
40. Dang, V.L.; Kieu, T.T.; Nguyen, T.T.T.; Truong, T.T.T.; Hoang, D.T.; Vu, T.L.C.; Nguyen, T.M.T.; Le, T.S.; Doan, T.H.Y.; Pham, T.D. Surface Modification of Zeolite by Cationic Surfactant and the Application on Adsorptive Removal of Azo Dye Ponceau 4R. *J. Mol. Struct.* **2024**, *1304*, 137619. [[CrossRef](#)]
41. Tang, B.; Guo, D.; Li, Y.; Yang, H.; Huang, Y.; Li, H. Separation and Quantitation of Isomeric Caffeoylquinic Acids in Honeysuckle Products by Low-PH Microemulsion Electrokinetic Chromatography Using Tartrate as a Chiral Selector. *Anal. Methods* **2016**, *8*, 189–196. [[CrossRef](#)]
42. Renda, C.G.; Ruellas, T.M.D.O.; Malafatti, J.O.D.; Araújo, C.S.S.; Silva, G.L.d.; Figueira, B.A.M.; Quaranta, S.; Paris, E.C. A “Zero-Cost” Adsorbing Hydroxyapatite-Based Material from Amazon Fishery Waste for Water Remediation and Nutrient Release for Agriculture. *Physchem* **2023**, *3*, 34–60. [[CrossRef](#)]
43. Dominic, C.D.M.; Neenu, K.V.; Begum, P.M.S.; Joseph, R.; Rosa, D.d.S.; Duan, Y.; Balan, A.; Ajithkumar, T.G.; Soumya, M.; Shelke, A.; et al. Nanosilica from Averrhoa Bilimbi Juice Pre-Treated Rice Husk: Preparation and Characterization. *J. Clean. Prod.* **2023**, *413*, 137476. [[CrossRef](#)]
44. Erans, M.; Arencibia, A.; Sanz-Pérez, E.S.; Sanz, R. Amine-Bridged Periodic Mesoporous Organosilica Adsorbents for CO<sub>2</sub> Capture. *J. Environ. Chem. Eng.* **2023**, *11*, 111590. [[CrossRef](#)]
45. Jinde, P.D.; Gudiyawar, M.Y. Synthesis, Characterization, and Thermal Behavior of Silica Aerogel-Embedded PVDF-HFP Nanofibers. *J. Mater. Res.* **2024**, *39*, 1396–1410. [[CrossRef](#)]
46. Nzereogu, P.U.; Omah, A.D.; Ezema, F.I.; Iwuoha, E.I.; Nwanya, A.C. Silica Extraction from Rice Husk: Comprehensive Review and Applications. *Hybrid Adv.* **2023**, *4*, 100111. [[CrossRef](#)]
47. Sari Yilmaz, M.; Piskin, S. Evaluation of Novel Synthesis of Ordered SBA-15 Mesoporous Silica from Gold Mine Tailings Slurry by Experimental Design. *J. Taiwan Inst. Chem. Eng.* **2015**, *46*, 176–182. [[CrossRef](#)]
48. Fu, P.; Yang, T.; Feng, J.; Yang, H. Synthesis of Mesoporous Silica MCM-41 Using Sodium Silicate Derived from Copper Ore Tailings with an Alkaline Molted-Salt Method. *J. Ind. Eng. Chem.* **2015**, *29*, 338–343. [[CrossRef](#)]
49. Santana Costa, J.A.; Paranhos, C.M. Systematic Evaluation of Amorphous Silica Production from Rice Husk Ashes. *J. Clean. Prod.* **2018**, *192*, 688–697. [[CrossRef](#)]
50. Belviso, C.; Kharchenko, A.; Agostinelli, E.; Cavalcante, F.; Peddis, D.; Varvaro, G.; Yaacoub, N.; Mintova, S. Red Mud as Aluminium Source for the Synthesis of Magnetic Zeolite. *Microporous Mesoporous Mater.* **2018**, *270*, 24–29. [[CrossRef](#)]
51. Zhang, Y.; Han, H.; Wang, X.; Zhang, M.; Chen, Y.; Zhai, C.; Song, H.; Deng, J.; Sun, J.; Zhang, C. Utilization of NaP Zeolite Synthesized with Different Silicon Species and NaAlO<sub>2</sub> from Coal Fly Ash for the Adsorption of Rhodamine B. *J. Hazard. Mater.* **2021**, *415*, 125627. [[CrossRef](#)] [[PubMed](#)]
52. Maatoug, N.; Delahay, G.; Tounsi, H. Valorization of Vitreous China Waste to EMT/FAU, FAU and Na-P Zeolite Materials. *Waste Manag.* **2018**, *74*, 267–278. [[CrossRef](#)] [[PubMed](#)]
53. Sun, X.; Zhang, Q.; Li, S.; Zhang, Y.; Liu, M.; He, B.; Mei, Y.; Zu, Y. Maximizing the Utilization of Calcium Species in the Supercages of CaNa-FAU Zeolite for Efficient CO<sub>2</sub> Capture. *Chem. Eng. J.* **2024**, *481*, 148661. [[CrossRef](#)]
54. Bunmai, K.; Osakoo, N.; Deekamwong, K.; Kosri, C.; Khemthong, P.; Wittayakun, J. Fast Synthesis of Zeolite NaP by Crystallizing the NaY Gel under Microwave Irradiation. *Mater. Lett.* **2020**, *272*, 127845. [[CrossRef](#)]
55. Joseph, I.V.; Tosheva, L.; Doyle, A.M. Simultaneous Removal of Cd(II), Co(II), Cu(II), Pb(II), and Zn(II) Ions from Aqueous Solutions via Adsorption on FAU-Type Zeolites Prepared from Coal Fly Ash. *J. Environ. Chem. Eng.* **2020**, *8*, 103895. [[CrossRef](#)]
56. Sousa, D.N.R.; Insa, S.; Mozeto, A.A.; Petrovic, M.; Chaves, T.F.; Fadini, P.S. Equilibrium and Kinetic Studies of the Adsorption of Antibiotics from Aqueous Solutions onto Powdered Zeolites. *Chemosphere* **2018**, *205*, 137–146. [[CrossRef](#)]
57. Alsafari, I.A.; Munir, S.; Zulfiqar, S.; Saif, M.S.; Warsi, M.F.; Shahid, M. Synthesis, Characterization, Photocatalytic and Antibacterial Properties of Copper Ferrite/MXene (CuFe<sub>2</sub>O<sub>4</sub>/Ti<sub>3</sub>C<sub>2</sub>) Nanohybrids. *Ceram. Int.* **2021**, *47*, 28874–28883. [[CrossRef](#)]
58. Azadi, F.; Pourahmad, A.; Sohrabnezhad, S.; Nikpassand, M. Synthesis of Zeolite Y @ Metal–Organic Framework Core@shell. *J. Coord. Chem.* **2020**, *73*, 3412–3419. [[CrossRef](#)]
59. Bohács, K.; Fajtli, J.; Bokányi, L.; Mucsi, G. Control of Natural Zeolite Properties by Mechanical Activation in Stirred Media Mill. *Arch. Metall. Mater.* **2017**, *62*, 1399–1406. [[CrossRef](#)]
60. Mohana, S.; Sumathi, S. Agaricus Bisporus Mediated Synthesis of Cobalt Ferrite, Copper Ferrite and Zinc Ferrite Nanoparticles for Hyperthermia Treatment and Drug Delivery. *J. Clust. Sci.* **2023**, *35*, 129–142. [[CrossRef](#)]



61. Barola, C.E.C.; Dusaban, I.F.C.; Olegario-Sanchez, E.M.; Mendoza, H.D. The Effect on the Zeta Potential of Surface Modified Philippine Natural Zeolites (SM-PNZ) for the Adsorption of Anionic Solutions. *IOP Conf. Ser. Mater. Sci. Eng.* **2019**, *478*, 012039. [[CrossRef](#)]
62. Thommes, M.; Kaneko, K.; Neimark, A.V.; Olivier, J.P.; Rodriguez-reinoso, F.; Rouquerol, J.; Sing, K.S.W. Physisorption of Gases, with Special Reference to the Evaluation of Surface Area and Pore Size Distribution (IUPAC Technical Report). *Pure Appl. Chem.* **2015**, *87*, 1051–1069. [[CrossRef](#)]
63. Khakzad Siuki, M.M.; Bakavoli, M.; Eshghi, H. Eco-Friendly Magnetic Clinoptilolite Containing Cu(0) Nanoparticles (CuNPs/MZN): As a New Efficient Catalyst for the Synthesis of Propargylamines via  $A_3$  and  $KA_2$  Coupling Reactions. *Appl. Organomet. Chem.* **2018**, *32*, e4290. [[CrossRef](#)]
64. Tan, M.; Li, X.; Feng, Y.; Wang, B.; Han, L.; Bao, W.; Chang, L.; Wang, J. Fly Ash-Derived Mesoporous Silica with Large Pore Volume for Augmented  $CO_2$  Capture. *Fuel* **2023**, *351*, 128874. [[CrossRef](#)]
65. Avellaneda, G.L.; Denoyel, R.; Beurroies, I.  $CO_2/H_2O$  Adsorption and Co-Adsorption on Functionalized and Modified Mesoporous Silicas. *Microporous Mesoporous Mater.* **2024**, *363*, 112801. [[CrossRef](#)]
66. Patil, D.J.; Behera, S.N. Synthesizing Nanoparticles of Zinc and Copper Ferrites and Examining Their Potential to Remove Various Organic Dyes through Comparative Studies of Kinetics, Isotherms, and Thermodynamics. *Environ. Monit. Assess.* **2023**, *195*, 591. [[CrossRef](#)]
67. Amorim, C.O.; Mohseni, F.; Dumas, R.K.; Amaral, V.S.; Amaral, J.S. A Geometry-Independent Moment Correction Method for the MPMS3 SQUID-Based Magnetometer. *Meas. Sci. Technol.* **2021**, *32*, 105602. [[CrossRef](#)]
68. Paris, E.C.; Malafatti, J.O.D.; Sciena, C.R.; Junior, L.F.N.; Zenatti, A.; Escote, M.T.; Moreira, A.J.; Freschi, G.P.G.  $Nb_2O_5$  Nanoparticles Decorated with Magnetic Ferrites for Wastewater Photocatalytic Remediation. *Environ. Sci. Pollut. Res.* **2021**, *28*, 23731–23741. [[CrossRef](#)]
69. Zhu, X.; Ma, C.; Yuan, X.; Zhao, J.; Hou, X. Synthesis of Magnetic NaY Zeolite for Plasma Proteomics Application. *Mater. Today Commun.* **2023**, *35*, 106219. [[CrossRef](#)]
70. Belviso, C.; Agostinelli, E.; Belviso, S.; Cavalcante, F.; Pascucci, S.; Peddis, D.; Varvaro, G.; Fiore, S. Synthesis of Magnetic Zeolite at Low Temperature Using a Waste Material Mixture: Fly Ash and Red Mud. *Microporous Mesoporous Mater.* **2015**, *202*, 208–216. [[CrossRef](#)]
71. Zhang, L.; Guan, Q.; Tang, L.; Jiang, J.; Sun, K.; Manirafasha, E.; Zhang, M. Effect of  $Cu^{2+}$  and  $Al^{3+}$  on the Interaction of Chlorogenic Acid and Caffeic Acid with Serum Albumin. *Food Chem.* **2023**, *410*, 135406. [[CrossRef](#)] [[PubMed](#)]
72. Xu, X.; Song, K.; Guo, J.; Liu, S.; Zhou, X.; He, J. Adsorption Behavior of Amino Functionalized MCM-41 on Chlorogenic Acid from *Eucommia Ulmoides* Leaves. *J. Porous Mater.* **2023**, *30*, 71–81. [[CrossRef](#)]
73. Cheng, Y.; Xu, L.; Liu, C. NaP1 Zeolite Synthesized via Effective Extraction of Si and Al from Red Mud for Methylene Blue Adsorption. *Adv. Powder Technol.* **2021**, *32*, 3904–3914. [[CrossRef](#)]
74. Phouthavong, V.; Hagio, T.; Park, J.H.; Nijpanich, S.; Srihirunthanon, T.; Chantanurak, N.; Duangkhai, K.; Rujiravanit, R.; Chounlamany, V.; Phomkeona, K.; et al. Utilization of Agricultural Waste to Herbicide Removal: Magnetic BEA Zeolite Adsorbents Prepared by Dry-Gel Conversion Using Rice Husk Ash-Derived  $SiO_2$  for Paraquat Removal. *Arab. J. Chem.* **2023**, *16*, 104959. [[CrossRef](#)]
75. Vandervoort, A.R.; Arai, Y. Macroscopic Observation of Soil Nitrification Kinetics Impacted by Copper Nanoparticles: Implications for Micronutrient Nanofertilizer. *Nanomaterials* **2018**, *8*, 927. [[CrossRef](#)]
76. Gu, W.; Li, X.; Xing, M.; Fang, W.; Wu, D. Removal of Phosphate from Water by Amine-Functionalized Copper Ferrite Chelated with La(III). *Sci. Total Environ.* **2018**, *619–620*, 42–48. [[CrossRef](#)]
77. Hassan, A.F.; El-Naggar, G.A.; Braish, A.G.; El-Latif, M.M.A.; Shaltout, W.A.; Elsayed, M.S. Utilization of Synthesized Copper Ferrite/Calcium Alginate Nanocomposite for Adsorption and Photocatalytic Degradation of Malachite Green. *J. Inorg. Organomet. Polym. Mater.* **2024**, *34*, 190–206. [[CrossRef](#)]

**Disclaimer/Publisher's Note:** The statements, opinions and data contained in all publications are solely those of the individual author(s) and contributor(s) and not of MDPI and/or the editor(s). MDPI and/or the editor(s) disclaim responsibility for any injury to people or property resulting from any ideas, methods, instructions or products referred to in the content.